Summer 2020

# Understanding the deformation mechanisms in Ni-based superalloys with using crystal plasticity finite element method

Tianju Chen



Department: Materials Science and Engineering

# UNDERSTANDING THE DEFORMATION MECHANISMS IN NI-BASED SUPERALLOYS WITH USING CRYSTAL PLASTICITY FINITE ELEMENT METHOD

by

TIANJU CHEN

A DISSERTATION

Presented to the Faculty of the Graduate School of the

MISSOURI UNIVERSITY OF SCIENCE AND TECHNOLOGY

In Partial Fulfillment of the Requirements for the Degree

DOCTOR OF PHILOSOPHY

in

MATERIAL SCIENCES AND ENGINEERING

2020

Approved by

Dr. Caizhi Zhou, Advisor
Dr. Haiming Wen
Dr. Laura Bartlett
Dr. Joseph W. Newkirk
Dr. Stephen Gao

## PUBLICATION DISSERTATION OPTION

This dissertation consists of the following two articles that have been published or will be submitted for publication as follows:

Paper I, pages 20-57 would be subsequently submitted to the International Journal of Plasticity for Publication.

Paper II, pages 58-81 have been published in JOM on 26 July 2019.

# ABSTRACT

Ni-based superalloy is considered as a good candidate due to its excellent resistance to elevated temperature deformation for long term period application. Understanding the deformation and failure mechanisms of Ni-Based superalloys is very helpful for providing design guidelines for processing Ni-based superalloys. Experimental characterization indicates that the deformation mechanisms of Ni based superalloy is strongly microstructure dependent. Besides, damage transform from the void nucleation to the macro cracks by voids growth leading to the failure of the Ni-based superalloys are also showing strong microstructure sensitivity. Therefore, this work focuses on the prediction and comprehension of the deformation and void growth behavior in Ni based superalloy at different working conditions via crystal plasticity finite element modeling and simulation.

Physically based crystal plasticity frameworks were developed for newly Ni-based superalloy Haynes 282. It was found that dislocation shearing through the precipitates were acting as the main contributor to the strength of Haynes 282 at room temperature and $815^0C$. Our analysis of the creeping behavior of Haynes 282 exhibited that resistance of general climb replaced by the resistance induced by the deposited climb dislocation density. In addition, in the study of void growth behavior, our simulation results demonstrated that as the main loading axis perpendicular to the grain boundary (GB), voids grow more slowly on tilt GBs in bicrystals than those in single and bicrystals with twist GBs. And tilt GBs would promote the void grow into irregular shape.

# ACKNOWLEDGMENTS

First and foremost, I am grateful to my major advisor, Dr. Caizhi Zhou for his solid support, encouragement and guidance throughout my Ph.D. study at Missouri University of Science and Technology.

Secondly, I would also like to thank my other committee members, Dr. Haiming Wen, Dr. Laura Bartlett, Dr. Joseph W. Newkirk and Dr. Stephen Gao for their guidance and insightful suggestions. They provided important feedback on my research during my Ph.D. study.

Next, I want to thank my parents and my twin brother, for the endless love and support.

Finally, special thanks to my wife Shujing Dong, my upcoming baby Jason. You are the reasons make me a better me every single day during my Ph.D. study.

# TABLE OF CONTENTS

Page

PUBLICATION DISSERTATION OPTION ..... iii

ABSTRACT ..... iv

ACKNOWLEDGMENTS ..... v

LIST OF ILLUSTRATIONS ..... x

LIST OF TABLES ..... xiii

NOMENCLATURE ..... xiv

SECTION

1. INTRODUCTION ..... 1

1.1. REQUIREMENTS OF TURBINE ENGINES ..... 1

1.2. DEFORMATION MECHAMISMS OF NI-BASED SUPERALLOYS ..... 3

1.3. THE CREEP BEHAVIOR OF NI-BASED SUPERALLOYS ..... 13

1.4. RESEARCH OBJECTIVES ..... 16

2. CRYSTAL PLASTICITY FINITE ELEMENT METHOD ..... 17

PAPER

I. PREDICTING THE HIGH TEMPERATURE DEFORMATION BEHAVIOR OF NI-BASED SUPERALLOYS BY A DISLOCATION-DENSITY BASED CRYSTAL PLASTICITY MODEL ..... 20

ABSTRACT ..... 20

1. INTRODUCTION ..... 21

2. MODELING APPROACH ..... 25

2.1. CONSTITUTIVE LAW ..... 25

2.2. TENSILE CONDITION ..... 26

2.2.1. Dislocation Interaction in the Matrix. ..... 26

2.2.2. Inter-particle Spacing. ..... 28

2.2.3. Effective Obstacle Spacing. ..... 29

2.2.4. Precipitation Shearing Model. ..... 30

2.2.5. Orowan Bypassing Model. ..... 31

2.2.6. Solid Solution Strengthening ..... 31

2.2.7. Tensile Shear Rate. ..... 33

2.3. CREEP CONDITIONS ..... 34

2.3.1. Climb Model ..... 34

2.3.2. $\gamma'$ Precipitates Coarsening. ..... 36

2.3.3. Climb Controlled Shear Rate. ..... 36

2.4. MODEL CALIBRATION ..... 37

3. RESULTS AND DISCUSSION ..... 40

3.1. EFFECT OF TEMPERATURE ON TENSILE PERFORMANCE OF HAYNES 282 ..... 40

3.2. DOMINANCE OF EFFECTIVE SPACING ..... 43

3.3. EFFECT OF $\gamma'$ PRECIPITATES SIZE ..... 45

3.4. EFFECT OF $\gamma'$ VOLUME FRACTION ..... 47

3.5. CREEP BEHAVIOR ..... 48

3.6. CLIMB CONTRIBUTION DURING CREEP ..... 49

3.7. EFFECT OF PARTICLES COARSENING ..... 52

4. CONCLUSIONS ..... 53

ACKNOWLEDGMENTS ..... 54

REFERENCES ..... 54

II. CRYSTAL PLASTICITY MODELING OF VOID GROWTH ON GRAIN BOUNDARIES IN NI-BASED SUPERALLOYS ..... 58

ABSTRACT ..... 58

1. INTRODUCTION ..... 59

2. METHODOLOGY ..... 62

3. RESULTS AND DISCUSSION ..... 67

3.1. VOID GROWTH IN SINGLE CRYSTALS ..... 67

3.2. VOID GRIWTH ON GBS IN BICRYSTALS ..... 68

3.3. PLASTIC DEFORMATION OF BICRYSTALS WITH VOIDS ..... 70

3.3.1. Accumulated Shear Strain on Slip Systems. ..... 70

3.3.2. Lattice Rotation During Void Growth ..... 72

3.3.3. Effective Schmid Factors. ..... 75

3.4. VOID SHAPE AND EQUIVALENT PLASTIC STRAIN DISTRIBUTION. 76

4. CONCLUSIONS ..... 78

ACKNOWLEDGMENTS ..... 79

REFERENCES ..... 79

SECTION

3. CONCLUSIONS AND RECOMMENDATIONS ..... 82

3.1. CONCLUSIONS ..... 82

3.2. FUTURE WORKS ..... 84

BIBLIOGRAPHY ..... 86

VITA ..... 89

# LIST OF ILLUSTRATIONS

SECTION Page

Figure 1.1. Cross section of a gas turbine engine. ..... 1

Figure 1.2. Images of failed turbo engine occurring in service. ..... 2

Figure 1.3. Evolution of the turbine entry temperature and the corresponding fuel consumption of engines since 1970. ..... 3

Figure 1.4. Images of the γ-γ' structure. ..... 4

Figure 1.5. Schematic of the coherency strain owing to the lattice misfit of phase a and phase b. ..... 5

Figure 1.6. Dark field TEM images of Haynes 282 showing the fine spherical γ' precipitates. ..... 6

Figure 1.7. Dark field TEM micrograph of IN718 showing the spherical $\gamma'$ from oblate $\gamma''$ phases as agglomerated in the center. ..... 7

Figure 1.8. Micrograph of δ-phase nucleated on the GB. ..... 8

Figure 1.9. Standard 2-step aging heat treatment of Haynes 282. ..... 9

Figure 1.10. Microstructures of the Haynes 282 subjected to the standard 2-step heat treatment. ..... 9

Figure 1.11. TEM images showing that dislocations shear through the γ' phase in pairs. 12

Figure 1.12. Schematic of the dislocation pairs configurations in the case of (a) weak pair-coupling and (b) strong pair-coupling. ..... 13

Figure 1.13. Creeping strain curve as the creeping time. ..... 14

Figure 1.14. Deformed specimen showing the deposited dislocation at the γ-γ' interface. ..... 15

Figure 1.15. Crack propagation in the SRR99 superalloy during deformation. ..... 15

Figure 2.1. Graphic of elastic-plastic decomposition in crystal plasticity theory ..... 18

PAPER I

Figure 1. Schematic of the initial finite element mesh. ..... 38

Figure 2. (a) Comparison between simulated and experimental tensile stress-strain curve at RT and 815℃ with an applied shear strain rate of $1\times10^{-4}$ $s^{-1}$(b) Comparison between simulated and experimental creep curves subjected to different tensile stress 190MPa, 241MPa, 310Mpa at 760℃. (c) Comparison between simulated and experimental creep curves subjected to different tensile stress 186MPa, 241MPa at 788℃. ..... 39

Figure 3. Comparison of the flow stress at strain level of 0.05 between RT and 815℃.. 42

Figure 4. Distribution of the contribution of different strengthening mechanisms at RT and 815℃. ..... 42

Figure 5. Evolution of the (a) forest dislocation density and (b) mobile dislocation density at RT and 815℃. ..... 43

Figure 6. Evolution of the effective spacing with various competing obstacle spacing during the tensile deformation at (a), (b) RT and (c), (d) 815℃..... 45

Figure 7. Stress-strain curve of Haynes 282 at RT and 815℃. ..... 46

Figure 8. Evolution of deposited climb dislocation density with and without considering particle coarsening at (a) 760 ℃ and (b) 788 ℃. ..... 50

Figure 9. Pie charts displaying each component to the total climb resistance at different stage during creep, with General Climb (blue color) and Deposited Dislocation Network (yellow color) at (a) 760 ℃ and (b) 788 ℃..... 51

Figure 10. Creep strain curve of Haynes 282 with precipitates coarsening (solid lines) and without precipitates coarsening (dash lines) at 760 ℃ and (b) 788 ℃.... 52

PAPER II

Figure 1. The initial finite element mesh for void growth calculations. ..... 66

Figure 2. (a) Evolution of the void volume fraction $f/f_0$ versus macro-equivalent strain for void in single crystal under different stress triaxiality levels, T. Distribution of equivalent plastic strain around the void in single crystal samples at $E_e = 0.2$ under (b) $T = 0.33$, (c) $T = 0.5$, (d) $T = 1.0$ and (b) $T = 2.0$. ..... 68

Figure 3. Evolution of the void volume fraction $f/f_0$ versus macro-equivalent strain for void in single crystal and in bicrystal at different stress triaxiality level. ..... 69

Figure 4. The ratio of the difference between the void volume fractions in bicrystal, $V_{\text{bicrystal}}$, and single crystal, $V_{\text{single crystal}}$, to the void volume fraction of single crystal at $E_e = 0.2$. ..... 70

Figure 5. Accumulated shear strain of each slip system versus normal Schmid Factor at $E_e = 0.2$ for different stress triaxiality level. ..... 71

Figure 6. Distribution of misorientation angles of elements at $E_e = 0.2$ in (a) single crystal samples, (b) bicrystal samples for T = 0.33 and (c) T = 1.0. ..... 74

Figure 7. Effective Schmid Factors for each slip system versus normal Schmid Factors at $E_e = 0.2$ for (a) T = 0.33, (c) T = 0.5, (d) T = 1.0 and (b) T = 2.0. ..... 75

Figure 8. Distribution of equivalent plastic strain around deformed voids at $E_e = 0.2$ for (a) T = 0.33 and (b) T = 1.0. ..... 77

# LIST OF TABLES

PAPER I Page

Table 1. Solid solution strengthening coefficients for different elements and concentration of solute elements in the matrix of Haynes 282. ..... 32

Table 2. Parameters of dislocation-density based CPFE model for tensile and creep behavior of Haynes 282. ..... 39

Table 3. Values of shearing stress and forest dislocation density induced stress with the effective spacing at different temperature for multiple precipitate size. ..... 46

PAPER II

Table 1. Parameters used in CPFE model for IN718. ..... 64

# NOMENCLATURE

| Symbol | Description |
|---|---|
| $\delta$ | Lattice misfit of an alloy |
| $G$ | Shear modulus |
| $v$ | Poisson's ratio |
| $b$ | Burgers vector |
| $\lambda$ | Obstacle spacing |
| $\boldsymbol{F}$ | Total deformation gradient |
| $\boldsymbol{F}^*$ | Deformation gradient tensor prior to stretch |
| $\boldsymbol{F}^{\boldsymbol{p}}$ | Plastic transformation deformation gradient tensor |
| $\boldsymbol{F}^{\boldsymbol{e}}$ | Elastic deformation gradient tensor |
| $a_\gamma$ | Lattice parameter of matrix |
| $a_{\gamma'}$ | Lattice parameter of $\gamma'$ phase |
| $\gamma_{APB}$ | Anti-phase boundary energy |
| $\mathbf{L}^{\mathrm{p}}$ | Plastic velocity gradient |
| $\boldsymbol{V}^{\boldsymbol{e}}$ | Symmetric left elastic stretch tensor |
| $\boldsymbol{R}^{\boldsymbol{e}}$ | Rotation tensor |
| $\boldsymbol{d}$ | Deformation rate tensor |
| $\boldsymbol{w}$ | Rate of spin tensor |
| $\boldsymbol{\epsilon}^e$ | Elastic strain |
| $\overset{\nabla}{\boldsymbol{\epsilon}}^e$ | Gradient rate of the elastic strain |
| $\widetilde{\boldsymbol{D}}^p$ | Deformation rate in configuration with rotation |

| | |
|---|---|
| $\widetilde{\boldsymbol{\Omega}}^{e}$ | Elastically lattice spin with rotation |
| $\overline{\boldsymbol{D}}^{p}$ | Deformation rate in configuration without rotation |
| $\overline{\boldsymbol{W}}^{p}$ | Rate of spin tensor without rotation |
| $\boldsymbol{\tau}$ | 2nd Piola-Kirchhoff stress |
| $\tilde{\mathbb{C}}^{\boldsymbol{e}}$ | Fourth-order anisotropic crystal elasticity tensor |
| $\dot{\gamma}^{\alpha}$ | Shear strain rate in slip system α |
| $\widetilde{\boldsymbol{Z}}^{\alpha}$ | Schmid tensor of slip system α |
| $\tau^{\alpha}$ | Applied shear stress in slip system α |
| $\tau_{p}$ | Applied shear stress on paired dislocation |
| $\Lambda_{1}$ | Lengths of the leading dislocations driving particle cutting |
| $\Lambda_{2}$ | Lengths of the trailing dislocations driving particle cutting |
| $F_{pair}$ | Dislocation pair force per unit length |
| $l_{1}$ | Segment lengths of dislocation pairs |
| $l_{2}$ | Segment lengths of dislocation pairs |
| $\tau_{Orowan}$ | Strength of dislocation Orowan looping |
| $\boldsymbol{B_0}$ | Initial undeformed configuration |
| $\boldsymbol{B}$ | Current deformed configuration |
| $\overline{\boldsymbol{B}}$ | Configuration by plastic distorting the crystal lattice |
| $\widetilde{\boldsymbol{B}}$ | Configuration by distorting the crystal lattice with elastically rotation |

| Acronyms | Description |
|---|---|
| CPFEM | Crystal Plastic Finite Element Method |
| Ni | Nickel |
| FCC | Face Centered Cubic |
| BCT | Body Centered Tetragonal |
| TEM | Transmission Electron Microscopy |
| SEM | Scanning Electron Microscopy |
| APB | Anti Phase Boundary |
| SADP | Selected Area Diffraction Pattern |
| GB | Grain Boundary |
| GBs | Grain Boundaries |
| Nb | Niobium |
| Al | Aluminum |
| Ti | Titanium |
| CRSS | Critical Resolved Shear Stress |
| RSS | Resolved Shear Stress |

# 1. INTRODUCTION

## 1.1. REQUIREMENTS OF TURBINE ENGINES

Gas turbines acting as one of the most important components in aircraft grain thrust by transforming chemical oil energy into acceleration power. A schematic illustration of the composition of turbine engine is shown in Figure 1.1 [1]. The compressed air generated from the compressor will be streamed into the combustion area, where it will be mixed with the fuel and ignited. The generating hot gas will be guided toward through a turbine, which extracts the mechanical work required to drive the compressor from the momentum change by accelerating the incoming air into an expressively higher velocity [2].

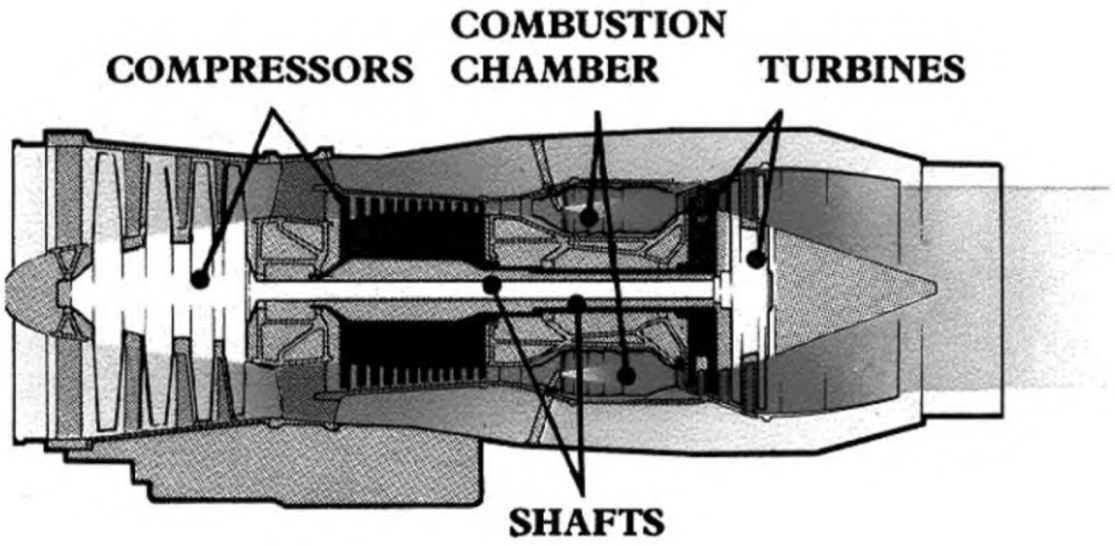


Figure 1.1. Cross section of a gas turbine engine [1].

Based on the prerequisites of these harsh working conditions, the selected materials need to possess desirable characteristics and capabilities to withstand higher pressure and temperature for long time period. Otherwise, the failure of components would occur that would cause tragic consequences. For example, Figure 1.2 displays a General Electrics CFM56 turbofan engine, which failed shortly after taking off in October, 2000. The failure was attributed to the segment loss of the turbine blades induced by the cracks propagation under the fatigue stress [2]. Painful apperception learned from these tragic circumstances emphasize that the performance and the reliability of the turbine engine relies profoundly upon the materials properties.

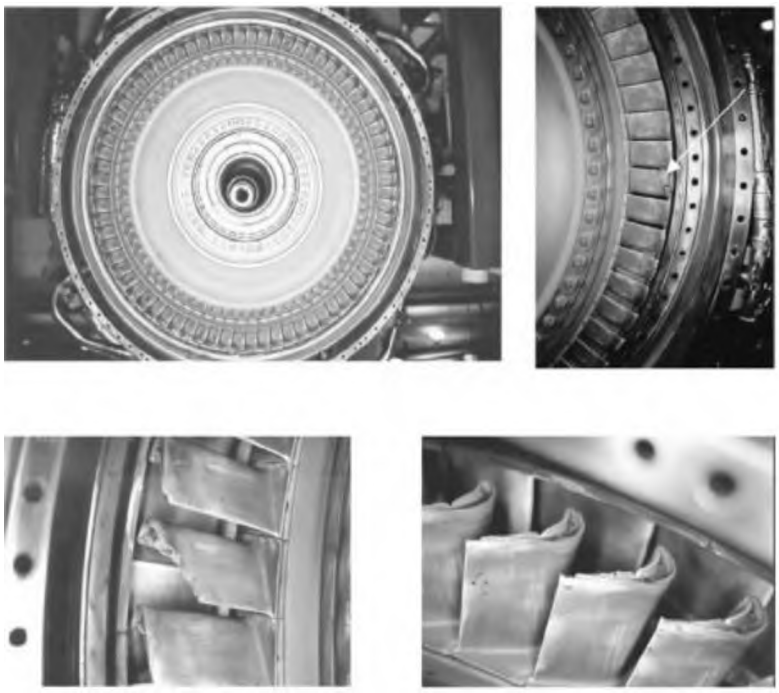

Figure 1.2. Images of failed turbo engine occurring in service [2].

What's more, over the past few decades, aircraft engines is growing the demand for the higher operating conditions driven by the efficiency increase and cost reduction. The development of the turbine entry temperature and the corresponding fuel consumption in

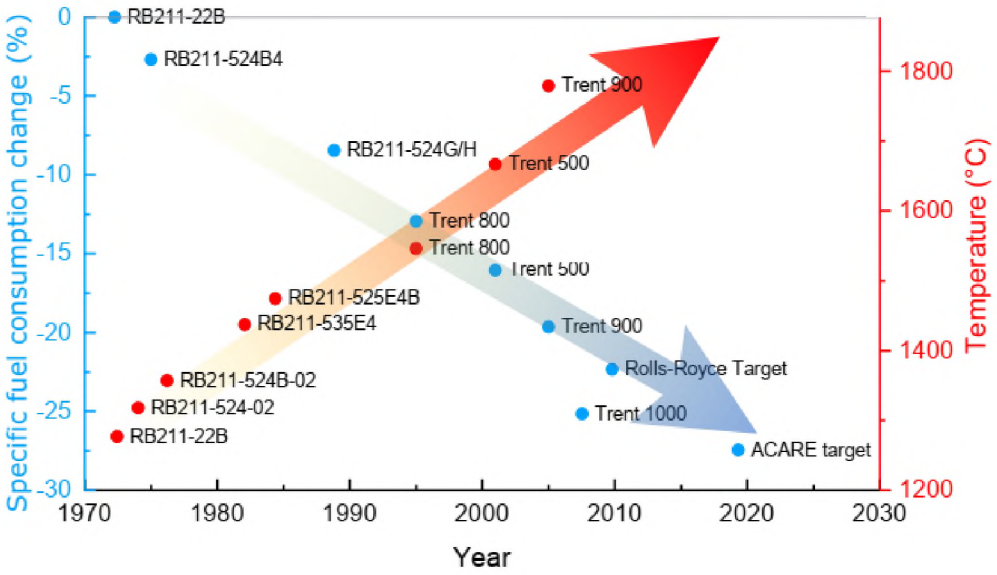


Figure 1.3. Evolution of the turbine entry temperature and the corresponding fuel consumption of engines since 1970 [3].

recent year are exhibited in Figure 1.3 [3]. As a consequence, the need of capability of materials to survive at more extreme conditions is budding.

## 1.2. DEFORMATION MECHAMISMS OF NI-BASED SUPERALLOYS

Ni-based superalloys are mainly consisting of two phases: face-centered cubic (FCC) $\gamma$ matrix and $\gamma'$ precipitates. The $\gamma$ matrix is comprised of Ni, Cr and other alloying elements while the $\gamma'$ phase is a coherent, ordered Ni3Al inter-metallic of $L1_2$ crystal structure and performs as distribution of precipitates as shown in Figure 1.4 [4, 5].

The $\gamma$ matrix is noted by the black arrow, displaying the channel of the matrix, and the phase with gray color represents the $\gamma'$ phase.

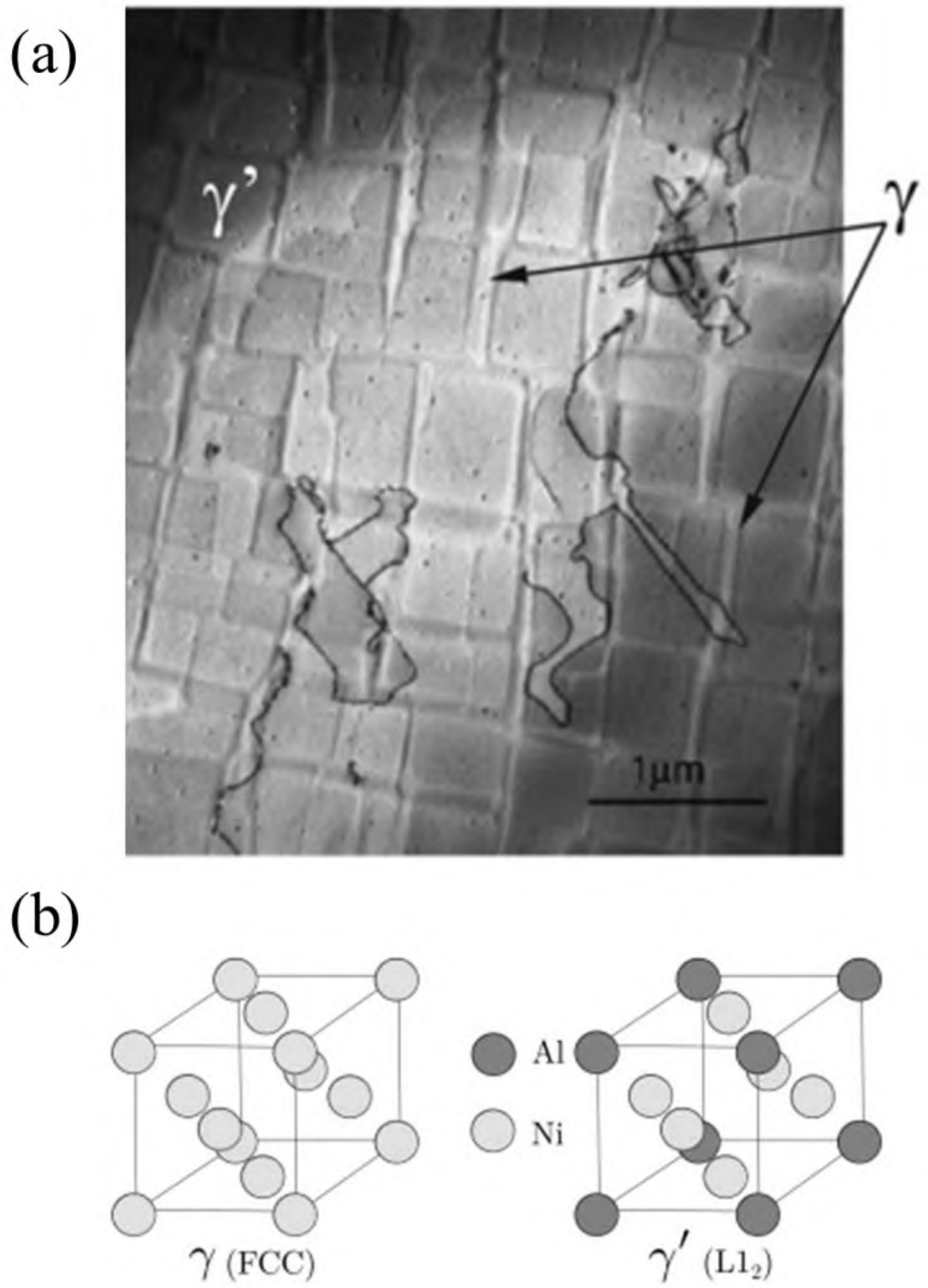


Figure 1.4. Images of the γ-γ' structure. (a) γ-γ' microstructure of CMSX-4 single crystal. (b) lattice crystal structure of FCC γ matrix (left) and L12 γ' precipitate (right) [4, 5].

Although the coherent interface between the $\gamma$ matrix and the $\gamma'$ precipitates, the lattice misfit still retained due to the slightly difference crystal structure among the $\gamma - \gamma'$ microstructure. The strain filed resulting from the lattice parameters misfit reinforce the strength by hindering the dislocation motion. Figure 1.5 exhibits the coherency strain owing to a lattice misfit between two different phases [6]. A key parameter is used to characterize the lattice misfit of an alloy shown as below [7]:

$$\delta = \frac{2\left(a_{\gamma'} - a_{\gamma}\right)}{a_{\gamma'} + a_{\gamma}} \quad (1)$$

therein, $a_{\gamma'}$ and $a_{\gamma}$ are representing lattice parameters of $\gamma'$ and $\gamma$ phase, respectively.

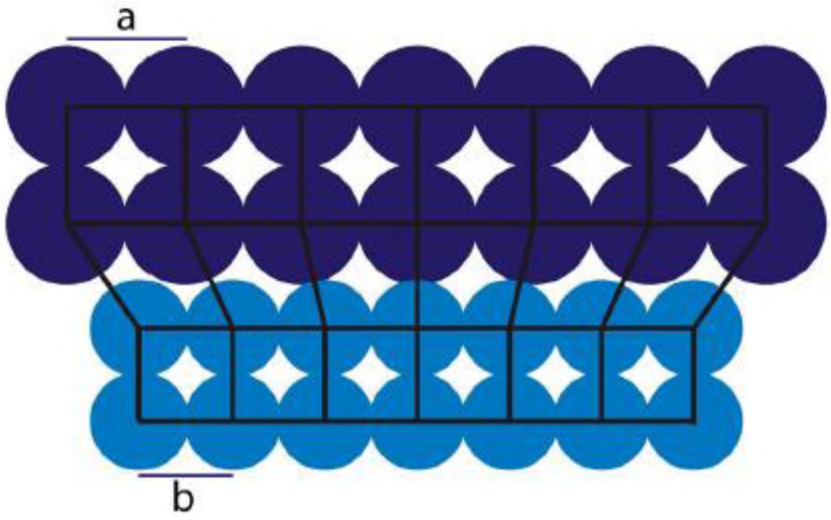


Figure 1.5. Schematic of the coherency strain owing to the lattice misfit of phase a and phase b [6].

Moreover, in most contemporary Ni-based single crystal superalloys, the volume fraction of the $\gamma'$ phase is about 70%, for example, like CMSX-4 [8]. However, some other Ni-based superalloys are only poessing small amount precipitation phase. In

contrast, early generation alloys such as Nimonic 90 is having about 20%-25% precipitation phase [9] and recent newly developed Ni-based superalloy Haynes 282 is maintaining approximate less than 20% volume fraction of $\gamma'$ segment as shown in Figure 1.6 [10, 11].

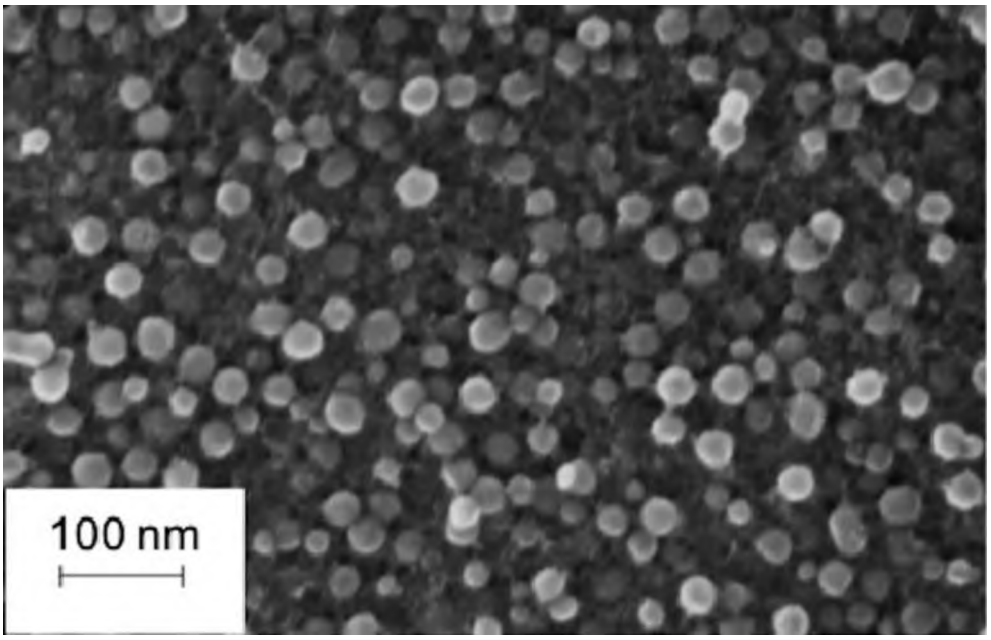


Figure 1.6. Dark field TEM images of Haynes 282 showing the fine spherical γ' precipitates [11].

Various volume fraction will stimulate different deformation mechanisms induced by the different dislocation behavior, resulting from the dissimilar $\gamma - \gamma'$ microstructure, such as channel width, particle morphology and so on.

In addition to the $\gamma - \gamma'$ microstructure, some Ni-based superalloys would also contain a secondary $\gamma'$ phase with size much smaller than the primary $\gamma'$, and the other phases such as δ, carbides and borides forming during the casting manufacturing process [7]. For instance, in polycrystalline Ni-based superalloys like IN718 as shown in Figure

1.7 [12], it is strengthened by the body-centered tetragonal (BCT) $\gamma'' - Ni_3(Al, Ti)$ and FCC $\gamma' - Ni_3(Nb)$ precipitates. Intermediate heat treatment will promote the nucleation of δ phase on the GB see Figure 1.8 [13]. The δ phase can stabilize and strengthen the GB by preventing the GB sliding. Then large $\gamma'$ and $\gamma''$ phases within the grain can balance the strength between GB and grains to improve the durability, ductility, and long-term high temperature stability [14, 15].

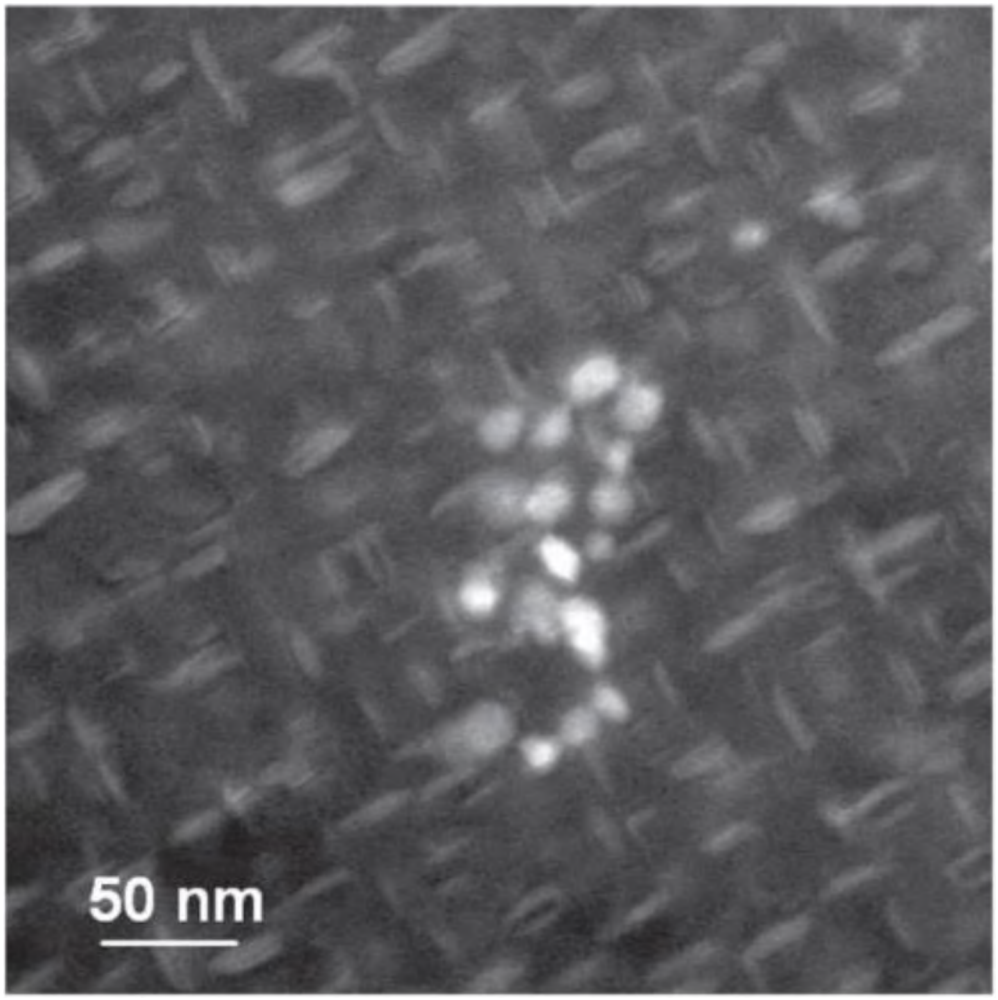


Figure 1.7. Dark field TEM micrograph of IN718 showing the spherical $\gamma'$ from oblate $\gamma''$ phases as agglomerated in the center [12].

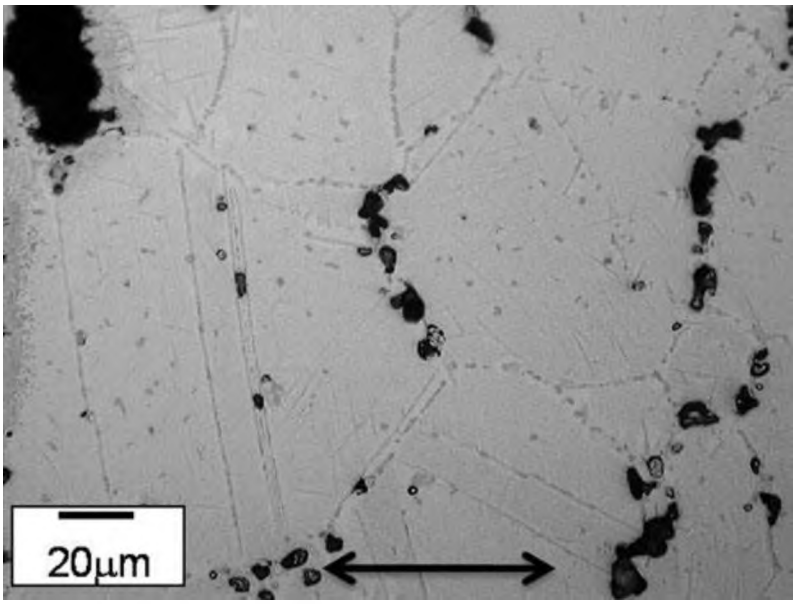


Figure 1.8. Micrograph of δ-phase nucleated on the GB [13].

Heat treatment has significantly influence on the performance of Ni-based superalloys as it controls the microstructural intelligence of Ni-based superalloys, including the distribution and morphology of constituent phases [10]. Figure 1.9 displays a standard heat treatment for Haynes 282, involving a 2-step aging process. In detail, the solution annealing treatment, at 1135℃ for 20 min, aims to dissolve precipitates such as carbides and $\gamma'$, and is kept short enough to avoid grain growth [16]. Water quench ensures the fast cooling rate to preserve the supersaturated solid solution structure of the alloy. The following 2-step aging aims for the optimum precipitation of GB carbides and fine $\gamma'$ particles, increasing the strength and creep resistance [10, 16]. Figure 1.10 displays the microstructure of Haynes 282 after the standard heat treatment, which contains precipitation of Cr-rich $M_{23}C_6$ and Mo-rich $M_6C$ carbides at GB improve the

creep strength and stability of the GB. And the pretty uniform distribution the $\gamma'$ particles help the material sustaining high strength for long term, high temperature deformation.

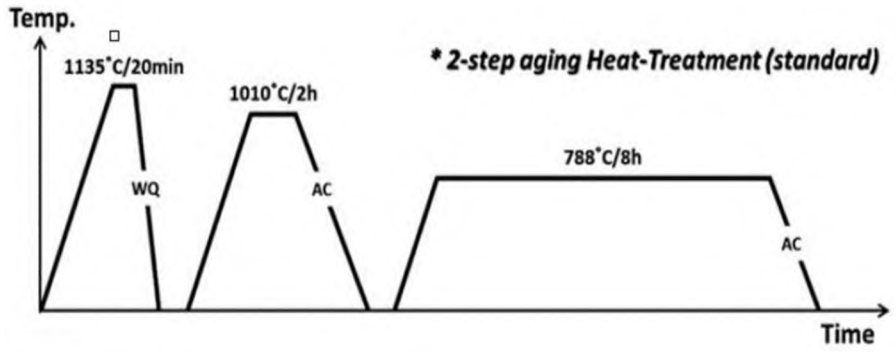


Figure 1.9. Standard 2-step aging heat treatment of Haynes 282 [16].

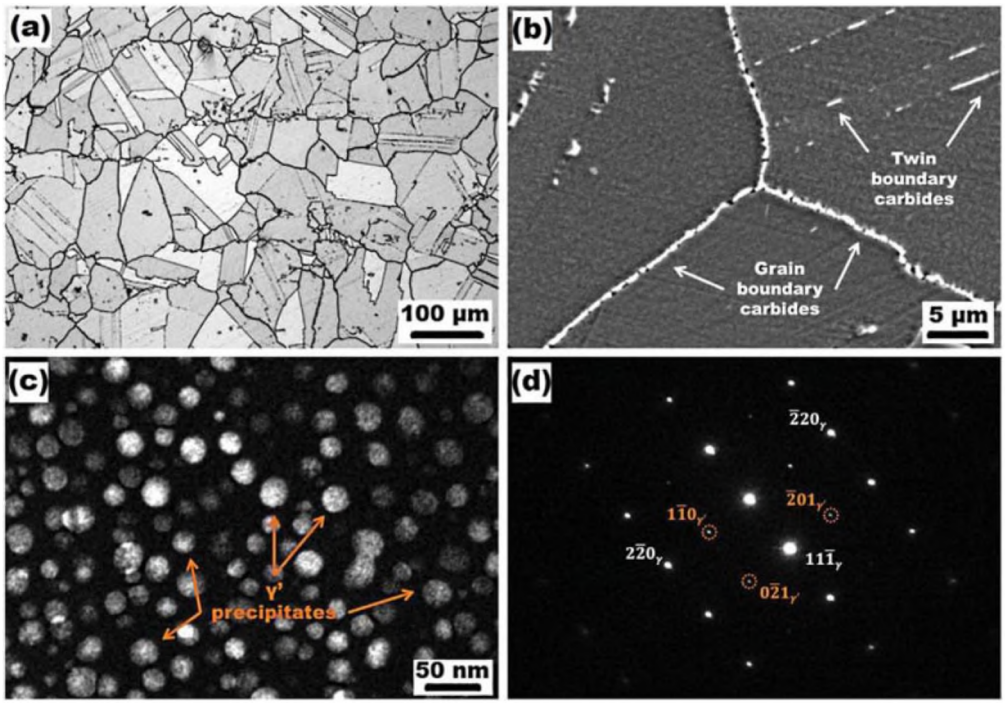


Figure 1.10. Microstructures of the Haynes 282 subjected to the standard 2-step heat treatment. (a) OM micrograph showing the grain size and traces of the rolling direction, (b) SEM images displaying homogeneous precipitation of M23 C6 and M6C carbides at GB, (c) Dark field TEM image of fine spherical $\gamma'$ particles, (d) SADP showing $\gamma$ matrix spots and superlattice pattern of the $\gamma'$ phase [16].

Before the failure of Ni-based superalloys, plastic deformation is mainly carried by the dislocation. Dislocations are gliding mainly in the matrix and will be interacted with other dislocations stored in the matrix. When the mobile dislocations meet some other held dislocations, the mobile dislocations will be hindered until the resolved shear stress (RSS) is large enough to overcome the resistance. As a consequence, more and more mobile dislocations will be pinned by the pioneer fixed dislocations, forming dislocation networks to further hamper gliding dislocations, until the RSS applied onto dislocations is larger than the critical resolved shear stress (CRSS), thereafter, dislocations will become transportable. In addition to the dislocations pinned by other dislocations, dislocations can also be stuck by other obstacles, like $\gamma'$ precipitate. Due to the difference of the hardness between the $\gamma$ and $\gamma'$ phases, dislocations motion is easily blocked inducing obvious accumulation of dislocations in the vicinity of $\gamma$ and $\gamma'$ interface. Both ways can help to increase the strength of Ni-based superalloys, as it need larger RSS to overcome the increased CRSS to accommodate the plastic deformation.

When dislocations interact with $\gamma'$ precipitates, they can either shear through the precipitates or looping around the precipitates [2]. The criterion on picking one or the other is dependent upon the size and volume fraction of the $\gamma'$ precipitate. In general, when precipitates are having small size, high volume fraction, and low anti-phase boundary (APB) energy, dislocations shearing through the particles are preferred [2]. It is well acknowledged that single $a/2 < 1\bar{1}0 > \{111\}$ dislocation in matrix cannot glide through the $\gamma'$ phase. Instead, dislocations shear through the precipitates must be in pairs with the formation of an APB, which has been demonstrated by TEM observation as shown in Figure 1.11 [2]. In detail, the first dislocation brings an APB when entering the

precipitates, and the second dislocation eliminates it, thereupon providing a resistance that need to be overcome when shearing occurring. In dislocations shearing through the $\gamma'$ particles, two situations are conceivable formed, noted as the weak and strong pair-coupling as shown in Figure 1.12 [17]. Generally, in the weak pair-coupling, it is considered that the leading dislocation has fully sheared the particles between two partial dislocations. In contrast, in the strong pair-coupling, the leading dislocation only partially sheared through the particles between two partial dislocations [17]. The critical hindrance of dislocation pairs shearing through the precipitates in Ni-based superalloys can be evaluated as result of the force balance between the repulsion force between the two partial dislocations and the force from the APB. The balance is dictated mathematically as [17-19]:

$$\tau_p b \Lambda_1 + F_{pair} \Lambda_1 - \gamma_{APB} l_1 = 0 \tag{2}$$

$$\tau_p b \Lambda_2 - F_{pair} \Lambda_2 + \gamma_{APB} l_2 = 0 \tag{3}$$

where $\tau_p$ is the applied shear stress, $\Lambda_1$ and $\Lambda_2$ are the lengths of the leading and trailing dislocations driving particle cutting, respectively. $F_{pair}$ is the dislocation pair force per unit length; and $\gamma_{APB}$ is the APB energy. $l_1$ and $l_2$ are the segment lengths of dislocation pairs.

Experimental characterization also has observed that the dislocation bypassed precipitates leaving dislocation loops around the $\gamma'$ particles. When the particle size is large enough, the volume fraction of the $\gamma'$ is relatively low, and the APB energy is high, dislocations looping around the $\gamma'$ particles during the deformation is favored. An empirical Orowan equation is used for evaluating the stress required for bowing a

dislocation between precipitates is dependent on the $\gamma'$ particles size and the interspacing of the $\gamma'$ particles [6]

$$\tau_{Orowan} = \frac{Gb}{\lambda} \tag{4}$$

where G is the shear modulus of the matrix, b is the Burgers vector and λ is the interspacing distance of the precipitates.

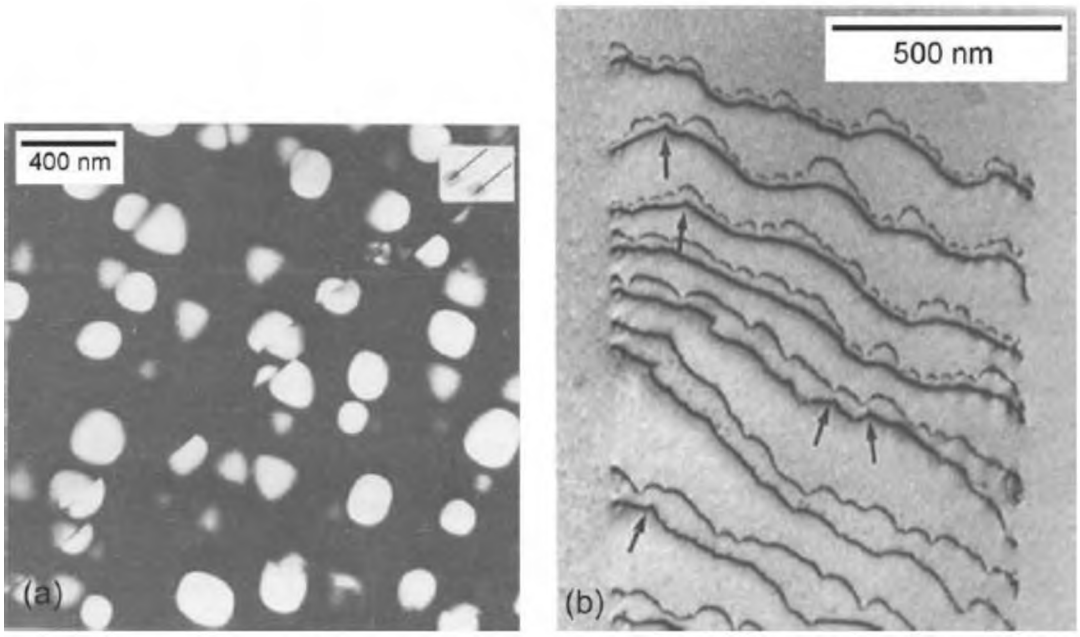


Figure 1.11. TEM images showing that dislocations shear through the γ' phase in pairs. (a) dark field micrograph of sheared particles in Nimonic 105; (b) pair of edge dislocations in Nimonic PE16 [2].

Due to the presence of different elemental additions sitting on the lattice sites of both $\gamma$ and $\gamma'$ phases, the crystal lattice is distorted around the substitutional solute atom [6].As a consequence, the distortions induced by the solid solutes make them interact with dislocations, making dislocations hard to move. Solid solution strengthening has pronounced influence on the strength of Ni-based superalloys, as some Ni-based

superalloys are having large volume fraction of alloying elements, and is strongly dependent on the chemical composition of the material [2].

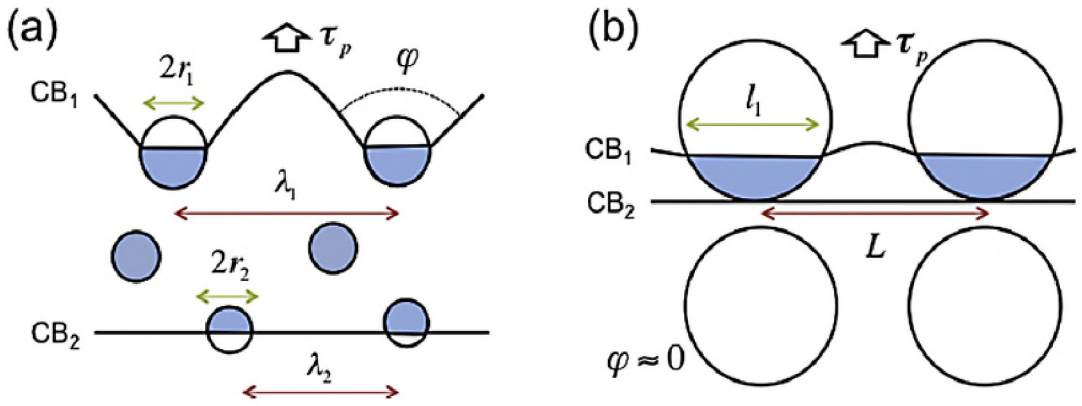


Figure 1.12. Schematic of the dislocation pairs configurations in the case of (a) weak pair-coupling and (b) strong pair-coupling [17].

## 1.3. THE CREEP BEHAVIOR OF NI-BASED SUPERALLOYS

During the service of turbine, it is subjected to a relatively lower stress but uphold for a long-term period during service. The loading stress is smaller than the yield strength of the materials. However, the plastic strain is accumulated over time, inducing failure of the turbine. Therefore, the creeping behavior of Ni-based superalloys determine the service life of the turbine engine. Creep is a time-dependent process, at constant stress and temperature [20]. Its period is usually consisting of three stages: primary, secondary, and tertiary as shown in Figure 1.13. During the primary stage, the creep strain rate is decreasing induced by the increase of the creep resistance during the deformation. For secondary creep, the creep rate reaches to a minimum value, as a result from the balance between the competing processes of straining hardening and recovery. Experimental characterization has observed that dislocations glide and climb are occurring during this

time and mainly within the $\gamma$ matrix [21]. It has been demonstrated that dislocation not only accumulate in the $\gamma$ phase, but also deposited at the interface of $\gamma - \gamma'$ as displayed in Figure 1.14 [21]. After transiting from secondary stage to tertiary stage, the creep strain starts to increase tremendously. In this period, damage begins to accumulate in the form of crack and voids. First, the voids are preferred to nucleate around the inclusions or the second phase, where it has large stress concentration. Next, the voids will start grow under the external loading condition. It is found that the local stress state around the voids has significant influence on the growth behavior of the voids [22]. Under loading, voids grow fast and coalesce with other neighbor voids, at the end forming the macroscopic cracks and fracture in the material. Consequently, the creep rate accelerates and quickens the materials to failure as shown in Figure 1.15 [23].

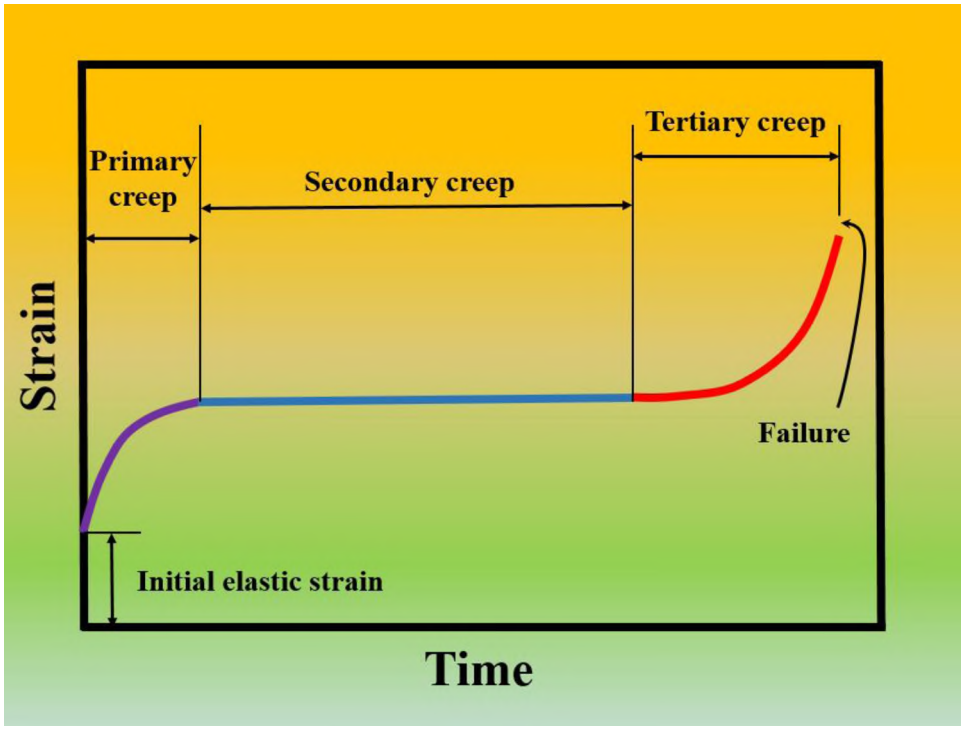


Figure 1.13. Creeping strain curve as the creeping time.

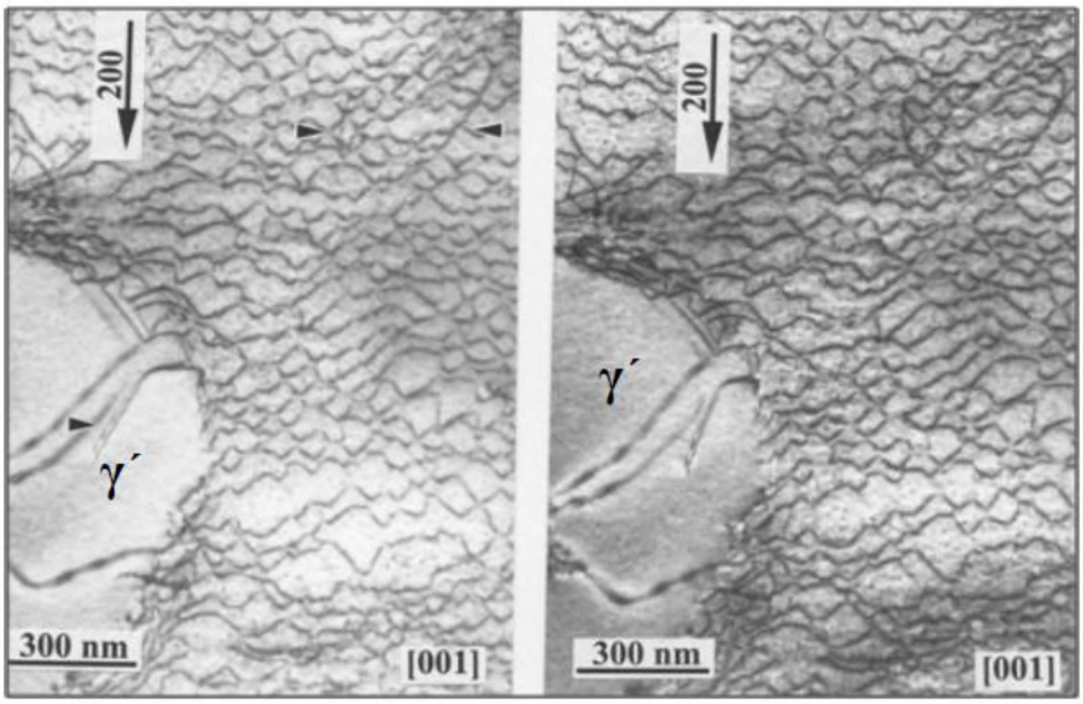


Figure 1.14. Deformed specimen showing the deposited dislocation at the γ-γ' interface [21].

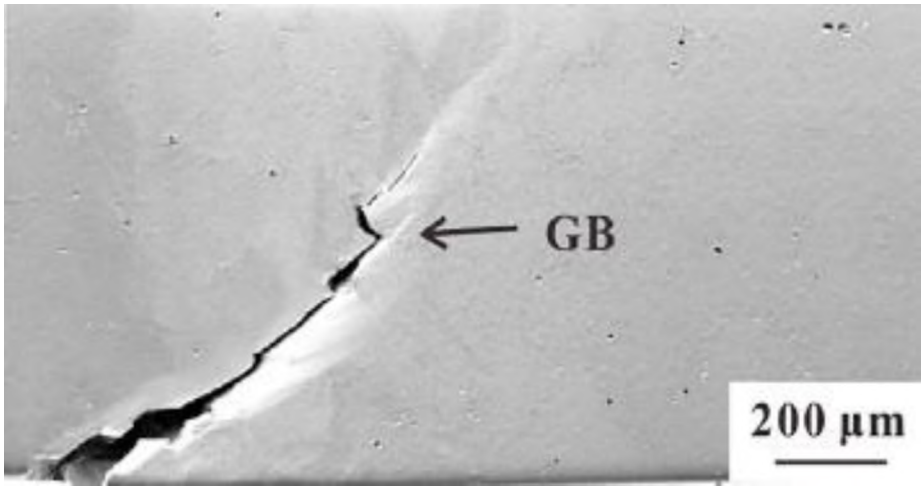


Figure 1.15**.** Crack propagation in the SRR99 superalloy during deformation [23].

## 1.4. RESEARCH OBJECTIVES

To design new advanced Ni-based superalloys with expected mechanical properties, the underlying deformation mechanisms must be fully understood. However, the slow progression of the experimental process, especially visually monitoring the long-term period deformation evolution makes it exhaustive and time-consuming. In recent decades, modeling approach are widely acknowledged as a powerful tool to establish the relationship between the microstructure-properties and the performance of the materials. Therefore, developing more reliable and comprehensive model that would be able to predict the mechanical performance of Ni-based superalloys is demanded to provide design guidelines for processing Ni-based superalloys with desired mechanical properties.

# 2. CRYSTAL PLASTICITY FINITE ELEMENT METHOD

Crystal plasticity finite element method (CPFEM), as a powerful technique bridging the macroscopic behavior of materials with the fundamental deformation mechanisms at the micro scale level, attracts a lot of attention in various application areas recently. Its applications are so broad that includes phase transformation, texture evolution, nanoindentation, pillar test, recrystallization and creep, damage, and fatigue, etc [24-26]. CPFEM allows the users to incorporate different constitute models dependent on their mechanisms including their interactions to study the size-dependent mechanical behavior. The output various of quantities from CPFEM can be compared with the finds of experiments in a very detailed manner.

In CPFEM theory, the total deformation gradient tensor **F** is multiplicatively decomposed as shown in Figure 2.1 into an elastic part $\boldsymbol{F^e}$, which includes the crystal lattice distortion and local rigid rotations and a plastic part $\boldsymbol{F^p}$ [7]:

$$\mathbf{F} = \boldsymbol{V^e F^*}, \boldsymbol{F^*} = \boldsymbol{R^e F^p} \tag{5}$$

The elastic component $\boldsymbol{F^e}$ is further decomposed into the symmetric left elastic stretch tensor $\boldsymbol{V^e}$ and the rotation tensor $\boldsymbol{R^e}$. During the plastic deformation, the major source of the plastic deformation is carried by the movement of dislocations. As the lattice retains its shape, the plastic part of the velocity gradient can be calculated based on its slip direction and slip plane normal associated to the lattice [27]. Consequently, the decomposition of the gradient induces two intermediate configurations denoted as $\bar{B}$ and $\tilde{B}$ between the initial undeformed configuration ($B_0$) and the current deformed configuration ($B$), as shown in Figure 2.1 [28]. Configuration $\bar{B}$ is defined by plastic

distorting the crystal lattice ($\boldsymbol{F^p}$) and $\tilde{B}$ is produced by further elastically rotation ($\boldsymbol{R^e}$) [28]. The constitutive model is developed based on the configuration $\tilde{B}$, which is obtained by freeing the elastic stretch from the deformed crystal $B$.

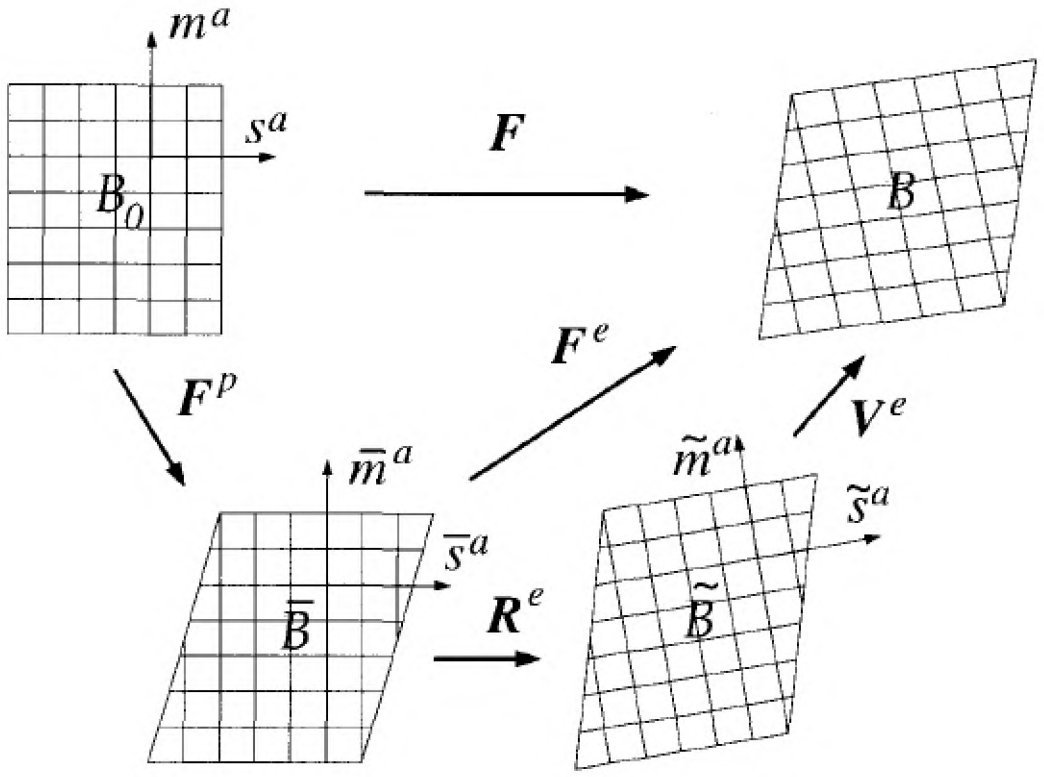


Figure 2.1. Graphic of elastic-plastic decomposition in crystal plasticity theory [28].

The constitutive model expressed with respect to the intermediate configuration $\tilde{B}$ can be summarized here [29]:

$$Kinematics:\ \boldsymbol{d} = \overset{\nabla}{\boldsymbol{\epsilon}}^e + \tilde{\boldsymbol{D}}^p,\ \overset{\nabla}{\boldsymbol{\epsilon}}^e = \dot{\boldsymbol{\epsilon}}^e + \boldsymbol{\epsilon}^e\tilde{\boldsymbol{\Omega}}^e - \tilde{\boldsymbol{\Omega}}^e\boldsymbol{\epsilon}^e \tag{6}$$

$$\boldsymbol{w} = -skew\left(\dot{\boldsymbol{\epsilon}}^e\boldsymbol{\epsilon}^e\right) + \tilde{\boldsymbol{\Omega}}^e + \widetilde{\boldsymbol{W}}^p,\ \tilde{\boldsymbol{\Omega}}^e = \dot{\boldsymbol{R}}^e\boldsymbol{R}^{eT} \tag{7}$$

$$Elasticity:\quad \boldsymbol{\tau} = \tilde{\mathbb{C}}^e : \boldsymbol{\epsilon}^e \tag{8}$$

$$Plasticity:\ \ \widetilde{\boldsymbol{D}}^{p} = \boldsymbol{R}^{e}\overline{\boldsymbol{D}}^{p}\boldsymbol{R}^{eT} = \sum_{\alpha=1}^{N}\dot{\gamma}^{\alpha}sym\left(\widetilde{\boldsymbol{Z}}^{\alpha}\right) \tag{9}$$

$$\widetilde{\boldsymbol{W}}^{p} = \boldsymbol{R}^{e}\overline{\boldsymbol{W}}^{p}\boldsymbol{R}^{eT} = \sum_{\alpha=1}^{N}\dot{\gamma}^{\alpha}skew\left(\widetilde{\boldsymbol{Z}}^{\alpha}\right) \tag{10}$$

$$\dot{\gamma}^{\alpha} = \Phi(\tau^{\alpha}) \tag{11}$$

$$\tau^{\alpha} = \boldsymbol{\tau}{:}\, sym\left(\widetilde{\boldsymbol{Z}}^{\alpha}\right) = \boldsymbol{\tau}{:}\,\widetilde{\boldsymbol{Z}}^{\alpha} \tag{12}$$

where $\boldsymbol{d}$ and $\boldsymbol{w}$ are the deformation rate and the rate of spin tensor, $\boldsymbol{\epsilon}^{e}$ is the elastic strain, $\overset{\nabla}{\boldsymbol{\epsilon}}^{e}$ is the gradient rate of the elastic strain. $\widetilde{\boldsymbol{D}}^{p}$ and $\widetilde{\boldsymbol{\Omega}}^{e}$ are the deformation rate and the elastically lattice spin, respectively. $\widetilde{\boldsymbol{W}}^{p}$ is the plastic part of the spin tensor. $\overline{\boldsymbol{D}}^{p}$ and $\overline{\boldsymbol{W}}^{p}$ are the rate of deformation and spin tensors without rotation, $\boldsymbol{\tau}$ is the 2nd Piola-Kirchhoff stress, $\tilde{\mathbb{C}}^{\boldsymbol{e}}$ is a fourth-order anisotropic crystal elasticity tensor. $\dot{\gamma}^{\alpha}$ is the shear strain rate in slip system α, $\widetilde{\boldsymbol{Z}}^{\alpha}$ represents the Schmid tensor of slip system α, and $\tau^{\alpha}$ is the applied shear stress in slip system α [29].

# PAPER

## I. PREDICTING THE HIGH TEMPERATURE DEFORMATION BEHAVIOR OF NI-BASED SUPERALLOYS BY A DISLOCATION-DENSITY BASED CRYSTAL PLASTICITY MODEL

Tianju Chen[1], Caizhi Zhou[2,*]

[1] Department of Materials Science and Engineering, Missouri University of Science and Technology, Rolla, MO 65409, USA

[2] Department of Mechanical Engineering, University of South Carolina, Columbia, SC 29201, USA

## ABSTRACT

Mechanical behavior of Ni-based superalloys is heavily dependent upon the microstructure state, calling for mesoscale model to study the relationship between the underlying microstructure and macroscopic performance. In this work, we employ crystal plasticity finite element method (CPFEM) to explore the deformation mechanisms of Hanyes 282 during short-term and long-term tests. Haynes 282 is a newly developed Ni-based superalloy, containing relatively low volume fraction (< 20%) of spherical $\gamma'$ precipitate phase. A dislocation-density based model is developed to describe the tensile and the creep behavior. Dislocation-particle interaction is incorporated of either Orowan looping or shearing through the $\gamma'$ precipitates at tensile condition. At creep condition, glide-climb combined dislocation behavior is integrated. A novel climb model based on deposited climb dislocation density is proposed in this work, accounting for the accumulation of the dislocation during the climb process. Predicted tensile stress-strain at

various temperature levels and creep strain responses at different stress levels and temperature levels are showing good agreement with corresponding experimental results. Analysis of the results indicates that dislocation shearing through the $\gamma'$ precipitates is acting as the main contributor to the strength of Haynes 282 at both room temperature (RT) and elevated temperature. Both relatively larger stress and higher temperature are promoting the dislocation climb process over the $\gamma'$ precipitates during the creeping, inducing higher deposited climb dislocation density.

**Keywords**: Crystal Plasticity, Dislocations, Strength, Finite element model

## 1. INTRODUCTION

Ni based superalloy are widely considered as the appropriate candidates for the application under ultra-supercritical condition, such as gas turbines in aerospace and steam generating power stations, due to their excellent performance at the extreme harsh working conditions [1]. Such superior mechanical properties are essentially contributed from $\gamma'$ phase which act as the distribution of the precipitations within the $\gamma$ matrix and also the carbide phase nucleate at the grain boundary (GB). Thence studies of Ni based superalloy has got a lot of attractions over decades. Reed et al. research [1] has a great contribution to the development of Ni based superalloys, not only addressing the physical metallurgy of Ni based superalloys including the strengthening effects and the defects evolutions during the deformation but also providing guidelines for its various applications like turbine blade and turbine discs. Computational tools are also playing important roles in understanding and designing Ni based superalloys. Ghosh et al. [2]

developed a homogenized, activation energy-based crystal plasticity model incorporating characteristic parameters of the subgrain scale $\gamma$–$\gamma'$ morphology to account for the subgrain microstructure. Reed et al. [3] proposed a model of the yield strength of Ni based superalloys based on chemical composition with using CALPHAD. Rabbe et al. [4] took advantage of dislocation dynamics method studying the importance of the dislocation glide and climb of high temperature and low stress creep of Ni based superalloy. Ali et al. [5] determined the role of coherency loss on rafting of superalloys by considering the internal misfit under high temperature low stress creep conditions with using phase-field crystal plasticity simulations.

Even though the understanding of Ni-based superalloys is more and more comprehensive based on a number of studies have been performed on various aspects of Ni based superalloys, the demand of increasing efficiency drives the development of newly Ni based superalloy to satisfy higher temperature and pressure, and harsher working conditions [6]. Haynes 282 is one of the promising candidates combining long term creep strength, corrosion resistance and thermal stability at high temperature [7]. The conventional heat treatment of this alloy is solution annealing for 1 h in between 1121 °C and 1149 °C then followed by a two-step aging at 1010 °C/2 h/AC and 788 °C/8 h/AC [8]. The conventional heat treatment produces fine spherical $\gamma'$ precipitates and also promotes homogeneous carbide particles nucleate on GB [8]. Similar with most Ni-based superalloys, the mechanical properties of Haynes 282 are associated with the operative deformation mechanisms which is strongly dependent on the state of the microstructure. Therefore, understanding the mechanical behavior and the corresponding deformation mechanisms is imperative.

A number of investigations of Haynes 282 from various aspects have been performed. For example, the influence of heat treatment has been drawn attention as it controls the microstructural constituents, distribution and morphology of constituent phases [8, 9]. Joseph et al. [9] noticed that the introduction of a solution treatment at 1120 °C would cause the grain growth, and carbides precipitated during the 788°C aging rather than during the 1010 °C aging, forming coarser $\gamma'$ and interconnected carbides. The coarser $\gamma'$ significantly reduced the strength and the interconnected carbides caused a 50% reduction in the ductility. Shin [8] compared the conventional heat treatment with an alternative more economical,1-step aging treatment (800°C/4h) and found that the 1-step aging could also promoted approximately 20% of fine spherical γ' precipitates with a slightly smaller size.

Tensile deformation of Haynes 282 has been the focus of many recent studies. Zhang et al. [7] studied the tensile properties of Haynes 282 at various temperature from room temperature (RT) to 800 °C, and found that the yield strength remains almost unchanged up to 600 °C. Characterized sample displayed that the dominant deformation mechanisms transit from dislocation shearing through the precipitates to dislocation Orowan looping around the precipitates. Besides, Shin et al. [8] proved that different cooling rate has great influence on the tensile strength of Haynes 282 as it controls the critical particle size for the transition between the shearing and bypassing mode.

Long-term period creeping tests has been conducted by Song et al. [10] at 700 °C and 750°C. Coarsening of the γ' particles have been detected during the creep at both temperatures. Moreover, dislocation shearing through the precipitates then replaced by looping around the precipitates during the creep at relatively large applied stress level

were characterized. In contrast, at relatively low applied stress and high temperature, the dominate deformation mechanism became into dislocation gliding combined with dislocation climbing and forming dislocation network in the interface of $\gamma/\gamma'$ phase.

Even though the insights gained via experimental characterization technique, the origin of the temperature effect and the relationship between the microstructure and properties is not well understood. And also, it is really exhausting and low efficient to record the microstructure evolution during a long-term test through experimental approach. Computational method provides an alternative method to study the mechanical behavior of Haynes 282 in a detailed fashion, however, only few works have been conducted in the past. Therein, Wang et al. [11] combined a FFT-based elasto-viscoplasticity model with a phase-field (PF) model to study plastic deformation of Haynes 282 to account for the non-uniform distribution of the $\gamma'$ phase. PF was used to attain the microstructure after different heat treatment process and obtain a spatial details of $\gamma'$ microstructure instead of using empirical formula to estimate the inter-particle spacing. Nevertheless, the complexity of the microstructure evolution and the analysis of its relationship with the corresponding deformation mechanisms were missing.

In the present study, a physical based crystal plasticity framework is proposed to study the plastic deformation of Haynes 282. Crystal plasticity finite element (CPFE) models have served as powerful models for establishing the microstructure-property relationship and bridging the microscale property evolution with the macroscopic mechanical performance [12-15]. We apply it to both the tensile and creep tests at different temperature and applied stress levels to examine the effect of temperature and stress on the interaction between the dislocation and the $\gamma'$ precipitates and also explore

the origin of the evolution deformation mechanisms. The developed constitutive model incorporates most of the deformation mechanisms that have been characterized via experimental observation, whilst the transition of the deformation mechanisms is taken into account based on the critical activating stress to quantify the relationship between the deformation mode and the strength of Haynes 282 at various temperatures. We demonstrate that the calculations achieve agreement with the experimental tensile stress-strain curve and creep-strain curve at different temperature and applied stress levels.

# 2. MODELING APPROACH

## 2.1. CONSTITUTIVE LAW

Take advantage of the CPFE method which is based on the solution of stress equilibrium and strain compatibility, a rate-dependent elasto-viscoplastic constitutive model accounting for elastic and plastic deformation of crystals and the underlying kinematic relations developed by Marin et al. [16] is modified to accommodate a microstructure-based constitutive model in this work. The $\mathbf{L}^{\mathrm{p}}$ is the plastic velocity gradient is calculated by:

$$\mathbf{L}^{\mathrm{p}} = \sum_{\alpha=1}^{N} \dot{\gamma}^{\alpha} \boldsymbol{s}^{\alpha} \otimes \boldsymbol{m}^{\alpha} \tag{1}$$

where $N$ is total number of slip systems in a single crystal, $\dot{\gamma}^{\alpha}$ is the shear strain rate of slip system $\alpha$, $\boldsymbol{s}^{\alpha}$ and $\boldsymbol{m}^{\alpha}$ are the slip direction and slip plane normal of slip system $\alpha$, respectively, and $\boldsymbol{s}^{\alpha} \otimes \boldsymbol{m}^{\alpha}$ defines the Schmid tensor.

Haynes 282 shows significant sensitivity to its microstructure. Different $\gamma'$ volume fraction, varies $\gamma'$ precipitates size will possess contrasts level of strength and creep behavior, and also temperature will induce different interaction behavior between dislocations and dislocations, and dislocations and $\gamma'$ precipitates. In the next sections, different microstructure-based models will be discussed.

## 2.2. TENSILE CONDITION

**2.2.1. Dislocation Interaction in the Matrix.** Due to the relatively smaller volume fraction of $\gamma'$ precipitates of Haynes 282, plasticity is only active inside the γ matrix whereas the $\gamma'$ phase is considered as rigid and behaves elastically in the present study. It has been shown experimentally on a variety of Ni-base superalloy that dislocation is the dominant carrier during plastic deformation. To account for varies type of dislocation interaction in the γ matrix during the deformation, the forest dislocation density is calculated based on the thermodynamics of dislocation storage, which accumulates under straining as the difference between dislocation generation and removal rates [17]:

$$\frac{\partial \rho_{for}^{\alpha}}{\partial \gamma} = \frac{\partial \rho_{gen,for}^{\alpha}}{\partial \gamma} - \frac{\partial \rho_{rem,for}^{\alpha}}{\partial \gamma} = k_1 \sqrt{\rho_{for}^{\alpha}} - k_2(\dot{\varepsilon}, T)\rho_{for}^{\alpha} \tag{2}$$

where, $\rho_{gen,for}^{\alpha}$ is the trapped forest dislocation density and $\rho_{rem,for}^{\alpha}$ is the removed part in slip system α either as defects or by recovery, respectively. The parameter $k_1$ is a coefficient for statistical trapping of mobile dislocations and $k_2$ is a coefficient for removal of trapped dislocations. The latter is a function of temperature and strain rate and related to $k_1$ via:

$$\frac{k_2}{k_1} = \frac{\chi b}{g}\left(1 - \frac{kT}{\tau_D b^3}\ln\left(\frac{\dot{\varepsilon}}{\dot{r}}\right)\right) \tag{3}$$

where $k$ is the Boltzmann constant, $g$ is an effective activation enthalpy, $T$ is the temperature, $\tau_D$ is a drag stress, $\dot{\varepsilon}$ is the applied strain rate and $\dot{r}$ is a characteristic rate that is related to the number of attempts to overcome barriers to slip [18].

Due to the strain gradient induced by the mechanical incompatibility near the interface of γ-$\gamma'$ and in the vicinity of grain boundaries, GND has been assessed in previous work by Birosca et al. [19]. To consider this effect, the evolution of the GND density is calculated by the formula derived by Ma et al. [20]:

$$\dot{\rho}^{\alpha}_{GNDs} = \frac{1}{b}\left\|\nabla_{\mathrm{x}} \times (\dot{\gamma}^{\alpha}\mathbf{F}_P^T\,\mathbf{n}^{\alpha})\right\| \tag{4}$$

where the nabla operator $\nabla_{\mathrm{x}}$ is defined as the derivative with respect to the reference coordinate, and $\mathbf{F}_P^T$ is the irreversible plastic strain. During the calculation, $\dot{\rho}^{\alpha}_{GND}$, is decomposed into three groups: one group of screw dislocations with tangent vector parallel to the slip direction, $\mathbf{d}^{\alpha}$, the other two groups of edge dislocations with tangent vectors parallel to $\mathbf{n}^{\alpha}$ and $\mathbf{t}^{\alpha}$, respectively, and can be obtained by:

$$\dot{\rho}^{\alpha}_{GNDs} = 1/b[\nabla_{\mathrm{x}} \times (\dot{\gamma}^{\alpha}\mathbf{F}_P^T\,\mathbf{n}^{\alpha})]\cdot\,\mathbf{d}^{\alpha} \tag{5}$$

$$\dot{\rho}^{\alpha}_{GNDet} = 1/b[\nabla_{\mathrm{x}} \times (\dot{\gamma}^{\alpha}\mathbf{F}_P^T\,\mathbf{n}^{\alpha})]\cdot\,\mathbf{t}^{\alpha} \tag{6}$$

$$\dot{\rho}^{\alpha}_{GNDen} = 1/b[\nabla_{\mathrm{x}} \times (\dot{\gamma}^{\alpha}\mathbf{F}_P^T\,\mathbf{n}^{\alpha})]\cdot\,\mathbf{n}^{\alpha} \tag{7}$$

Finally, the change of GNDs, $\dot{\rho}^{\alpha}_{GND}$ is calculated by:

$$(\dot{\rho}^{\alpha}_{GND})^2 = (\dot{\rho}^{\alpha}_{GNDs})^2 + (\dot{\rho}^{\alpha}_{GNDet})^2 + (\dot{\rho}^{\alpha}_{GNDen})^2 \tag{8}$$

The slip resistance encountered by gliding dislocation can be calculated according by Taylor strain hardening law:

$$\tau_{\rho}^{\alpha} = \chi G b \sqrt{\rho_{for}^{\alpha} + \rho_{GND}^{\alpha}} \tag{9}$$

**2.2.2. Inter-particle Spacing.** For both creep and tensile deformations, the inter-particle spacing, $\lambda_p$, is a crucial microstructure parameter [2, 21, 22]. Most strength models of Ni-based superalloys are described as a function of $\lambda_p$. To acquire an appropriate $\lambda_p$, varies models have been developed, most of them assumed that the spacing between particles are simply the distance between the centers of particles in their work. In these studies, dislocations gliding planes are assumed to across the center plane of precipitates, which is too coincidence to happen in the real deformation process. Thus, a 3D to 2D conversion model is needed to get a precise magnitude of $\lambda_p$. In present study, we employ a dimension reduction procedure developed by Topuz [23] which has been proposed together with a 2D dislocation dynamics and has been successfully in predicting tensile response of materials under varies conditions. Here we only briefly introduce this dimension reduction procedure, for more detail, readers are referred to [23]. Assuming there are N precipitates with average radius of R inside a representative cubic volume of edge size W, the corresponding volume fraction can be obtained by:

$$P_{3D} = \frac{4}{3} N \pi \left(\frac{R}{W}\right)^3 \tag{10}$$

If m discs generated by slicing are present on a square with edge size of W, the fraction of total discs area are:

$$P_{2D} = m\pi \left(\frac{R^{2D}}{W}\right)^2 \tag{11}$$

The relation between R and $R^{2D}$ is determined by integrating the slicing step over the sphere:

$$R^{2D} \approx \frac{1}{\pi}\int_0^{\pi} Rsin\theta d\theta = \frac{2}{\pi}R \tag{12}$$

After performing infinite slices, the equivalent fraction between area fraction and the volume fraction can be expected:

$$P_{2D} = P_{3D} \tag{13}$$

After derivation, the number of discs in 2D can be expressed:

$$m = \frac{\frac{4}{3}NR^3}{WR^{2D^2}} \tag{14}$$

With the geometric relation of precipitates and square, one can easily obtain:

$$\lambda_p + 2R^{2D} = \frac{W}{\sqrt{m}} \tag{15}$$

Finally, the mean spacing of the $\gamma'$ precipitates $\lambda_p$ can be expressed:

$$\lambda_p = 1.64\, r_p\left(\sqrt{\frac{\pi}{4f}} - 1\right) \tag{16}$$

where $r_p$ is the radius of the precipitates, and $f_p$ is the volume fraction of $\gamma'$ phase.

**2.2.3. Effective Obstacle Spacing.** During the deformation of Hayne 282, the plastic strain is mainly carried by the mobile dislocation. Mobile dislocations are resisted by interior structure in the γ matrix including dislocation structure and $\gamma'$ precipitates, and are supposed to travel a mean free path $\lambda_{eff}$ before it is trapped or annihilated [17, 24]. As the development of various competing means trapping dislocation, $\lambda_{eff}$ is determined by the evolution of multiple obstacles including forest dislocation spacing, GND spacing, and the spacing of $\gamma'$ precipitates. To account for a multiple obstacles type interacts with moving dislocations, an effective obstacle spacing is developed [25]:

$$\frac{1}{\lambda_{eff}} = \frac{\beta_{for}}{\lambda_{for}} + \frac{\beta_{GND}}{\lambda_{GND}} + \frac{\beta_p}{\lambda_p} \tag{17}$$

where $\beta_{for}$, $\beta_{GND}$ and $\beta_p$ are constants relate to the spacing of forest dislocation, spacing of GND, and spacing of $\gamma'$ precipitates, respectively.

**2.2.4. Precipitation Shearing Model.** It is well identified that $\boldsymbol{\gamma'}$ shearing is one of the main contributors to the strength of Ni-based superalloy, the effect of the $\boldsymbol{\gamma'}$ shearing strength of Haynes 282 must be considered. The subject of $\boldsymbol{\gamma'}$ shearing has been studied for a long time, including of effect of $\boldsymbol{\gamma'}$ particle size, shape and volume fraction on the shearing strength. In present study, we employed a unimodal model developed by Galindo-Nava et al. [26], which combined the shearing mechanism controlled by weak or strong pair-coupling into a single equation.

The strength from shearing $\gamma'$ precipitates can be calculated:

$$\tau^{\alpha}_{shear} = \frac{\gamma_{APB}}{2b} * \frac{l}{\Lambda + d} \tag{18}$$

where $\gamma_{APB}$ is the anti-phase boundary energy of the $\gamma'$ phase, b is the Burgers vector, $l$ is average the segment length of the leading dislocation acting in the cutting of a particle, $\Lambda$ is the average effective length between the obstacles by leading dislocation. The average length of the leading dislocation cutting the precipitates $l$ can be obtain by:

$$l = \begin{cases} d & if\ d < d_m \\ (d^2 - (d - d_m)^2)^{1/2} & if\ d \geq d_m \end{cases} \tag{19}$$

where $d_m$ is the critical particle size at the transition from weak to strong pair coupling, which can be calculated as:

$$d_m = \frac{\mu b^2}{\gamma_{APB}} \tag{20}$$

The average effective length between the obstacles $\Lambda$ can be defined as:

$$\Lambda = \max\{\lambda, L-l\} = \max\{\frac{2T}{d\gamma_{APB}}^{\frac{1}{2}} * L, L-l\} \quad (21)$$

where $\lambda$ is the Friedel sampling length, which represents the mean distance between particles encountered by a bowing dislocation along its length [9]. $T = 0.5\mu b^2$ is the dislocation line tension, and L is the mean spacing of the particles.

**2.2.5. Orowan Bypassing Model.** Apart from shearing through the $\gamma'$ precipitates, looping around the precipitates has also been experimentally during the deformation. Previous studies have demonstrated that the content of the dislocation loops increases significantly as the temperature increase. The critical stress needed for Orowan looping decrease quickly with increasing temperature. Once the critical stress for Orowan looping is less than the stress for shearing the precipitates, the transition of the deformation mechanism is altered. The required stress for Orowan looping to prevail can be calculated based on particle size r and volume fraction $f_p$ [8]:

$$\tau^{\alpha}_{Orowan} = \frac{0.4Gb}{\pi\sqrt{1-\nu}} * \frac{\ln(\frac{2r}{b})}{\lambda_p} \quad (22)$$

where G, b are shear modulus, Burgers vector as defined before, and $\nu$ is Poisson ratio. $\lambda_p$ is the mean spacing of the particles.

**2.2.6. Solid Solution Strengthening.** Similar to most other Ni based superalloy, Haynes 282 contains many other different elements may sitting on the lattice sites of both the γ and $\gamma'$ phases. Distorted crystal lattice can be expected due to the misfit between the additions and the major element. And the induced strain fields interact with dislocation thereby further impeding the motions of dislocations increase the

strength. Felthman [27] proposed a model for calculated the solid solution strengthening based on alloying elements in materials given by [28, 29]:

$$\sigma_{ss} = (1 - f_p)[\sum_i \left(a_i c_i^{\frac{1}{2}}\right)^2]^{1/2} \quad (23)$$

where $c_i$ and $a_i$ are the concentration and strengthening constant for element i. The values of $c_i$ and $a_i$ are determined with the calculation of the equilibrium composition by Thermo-Calc based on the minimization of the Gibbs free energy of the system. And the composition of each element are listed in Table 1.

Table 1. Solid solution strengthening coefficients for different elements and concentration of solute elements in the matrix of Haynes 282.

| Alloy element | Concentration (at) | Strengthening Constant (MPa/at%) |
|---|---|---|
| Al | 0.98 | 225 |
| Co | 12.02 | 39.4 |
| Cr | 25.70 | 337 |
| Fe | 1.87 | 153 |
| Mn | 0.47 | 448 |
| Mo | 4.65 | 1015 |
| Ti | 0.35 | 775 |

**2.2.7. Tensile Shear Rate.** To account for the rate effects and temperature, in this work, we calculate shear strain for each slip system with using Orowan equation:

$$\dot{\gamma}^{\alpha} = {\rho_m}^{\alpha} b v^{\alpha} \tag{24}$$

where ${\rho_m}^{\alpha}$ is the mobile dislocation density on slip system α, b is burger's vector, $v^{\alpha}$ is the average dislocation glide velocity:

$$v^{\alpha} = {\lambda_{eff}}^{\alpha} v_0 \exp\left(\frac{-Q_s}{k_B T}\right) \sinh\left(\frac{\tau_{eff} V}{k_B T}\right) \tag{25}$$

where $k_B$ is the Boltzmann constant, T is the absolute temperature. ${\lambda_{eff}}^{\alpha}$ is the jump width of slip system α. $v_0$ is the attach frequency, $Q_s$ is the activation energy for dislocation slip, V is the activation volume, and can be obtained as:

$$V = b^2 {\lambda^{\alpha}}_{eff} \tag{26}$$

The average dislocation glide velocity $v^{\alpha}$ is dependent of the effective stress $\tau_{eff} = \tau - \tau'$. $\tau$ is the shear stress acting on the dislocation and $\tau'$ is the resistance stress, which is the summation of all the strengthening mechanism:

$$\tau' = \tau_{\rho} + \tau_{ss} + Min\{\tau_{Orowan}, \tau_{Shear}\} \tag{27}$$

The operative mechanism between Orowan loop and precipitates shearing is determined to be the one with smaller strength at instantaneous moment during the deformation.

By incorporating the strengthening mechanism described above into our model to simulate the tensile tests, the constitutive equation for the shear rate in γ matrix on slip system α can be written as:

$$\dot{\gamma}^{\alpha}_{slip} = \begin{cases} 0, & |\tau| < \tau' \\ \rho^{\alpha}_m b {\lambda^{\alpha}}_{eff} v_0 \exp\left(\frac{-Q_s}{k_B T}\right) \sinh\left(\frac{\tau_{eff} V}{k_B T}\right) sign(\tau^{\alpha}), & |\tau| \geq \tau' \end{cases} \tag{28}$$

## 2.3. CREEP CONDITIONS

Experimental characterization of crept Haynes 282 samples have demonstrated that the dominant deformation mechanisms of sample crept at low stress and high temperature level is dislocation gliding combined with dislocation climbing. Specifically, dislocation networks accumulated near the interface of $\gamma$ $\gamma'$ alter the direction of dislocation and promote the dislocation to climb over the $\gamma'$ particles. Nevertheless, the climbing process is much longer compared with the process of dislocation gliding in the matrix. Wherefore, escaping rate from the $\gamma'$ particles via climb is considered as the rate-controlling mechanism during this combined glide-climb process.

**2.3.1. Climb Model.** During the climbing process, the dislocation will be hiking onto the interface of $\gamma'$ particles by vacancy diffusion and forming a stable configuration under the action of its line tension. From previous studies, the stable dislocation profile is strongly dependent on the stress level. Wherein, two different climb modes were proposed to evaluate the stable contour, ie., local climb and general climb. For local climb, the dislocation line is confined closely to the particle interface with sharp bending corners, which is a preferred configuration at high applied stress. It has been evaluated by [30] that the stress required for stable local climb is as high as Orowan looping stress. Whereby, at an intermediate applied stress below the Orowan stress, the local climb is an energetically unstable process and therefore a "strictly" local climb process does not occur. In contrast, general climb occurs at relative low stress level with a lower strain rate, which permits vacancy diffusion to relax the dislocation profile to leave the particle interface, forming a smooth curve [30, 31]. Based on the minimum energy, the critical stress by forming equilibrium dislocation line can be obtained according to [30]:

$$\frac{\tau_{rc}}{\tau_{Orowan}} = \frac{\eta * r_p}{2 * \lambda_p} \tag{29}$$

And $\eta < 1$ is a spatial-distribution parameter to account for the local variance.

Quek [32] observed the loss of interface coherency around a misfitting inclusion during deformation with using dislocation dynamics method, and pointed out that the embedded particles could provide a barrier to dislocation motion as the cost of the interface coherency. In other words, climbed dislocations will be deposited on the particles inducing a "local dislocation network" creating resistance for the further motion of dislocation. To consider this hindrance, we developed a novel model to account for the looped dislocation via climb which impede the further dislocation climb.

The total climb dislocation density in the microstructure can be calculated based on the definition:

$$\rho_{climb} = L_{total}/V_{total} \tag{30}$$

where $L_{total}$ is the total climb dislocation length, and $V_{total}$ is the total climb dislocation occupied volume. Since the climb dislocation are all around the interface of the precipitates, the total volume can be given as:

$$V_{total} = \frac{N_p V_p}{f} \tag{31}$$

where $N_p$ is the number of the $\gamma'$ particles and $V_p$ is the volume fraction per spherical particle and $V_p = \frac{4}{3}\pi {r_p}^3$. For $L_{total}$, it can be calculated as defined:

$$L_{total} = N_p * N_{ff} * 2\pi r_p \tag{32}$$

where $N_{ff}$ is the product of the number of the attached dislocation via climb and the length fraction account for the dislocation loops not on the center plane of particles. In

our model, we assign $N_{ff}$ is an accumulated shear strain dependent parameter, which increase proportional to the accumulated shear strain:

$$\frac{\partial {N_{ff}}^{\alpha}}{\partial \gamma^{\alpha}} = k_3 \tag{33}$$

where $k_3$ is a fitting parameter. Finally, the evolution of the climb dislocation density bypassing the $\gamma'$ particles during the deformation can be shown:

$${\rho_{climb}}^{\alpha} = \frac{3 * {N_{ff}}^{\alpha} * f}{2 * {r_p}^2} \tag{34}$$

**2.3.2. $\gamma'$ Precipitates Coarsening.** The coarsening of $\gamma'$ precipitates has been detected in Crept Haynes 282 samples [10], which plays a really important role in determine the creeping life. Thus, it is necessary to consider the size change of $\gamma'$ precipitates due to the coarsening. The long term $\gamma'$ coarsening evolution can be described by the cubic law [33]:

$$D^3(t) - {D_0}^3(t_0) = K(T)(t - t_0) \tag{35}$$

where $D$ and $D_0$ are diameter of $\gamma'$ precipitates at time $t$ and $t_0$, respectively. And $K(T)$ is temperature dependent rate constant and can be calculated in the Arrhenius form:

$$K = K_0 \exp\left(-\frac{Q}{R_g T}\right) \tag{36}$$

where $Q = 313.2 kJ/mol$ is the activation energy, and $K_0 = 7.15 \times 10^{-14} m^3/sec$ is the pre-exponential factor of Haynes 282.

**2.3.3. Climb Controlled Shear Rate.** During climbing process, absorption and emission of vacancies from dislocations results in the formation of jogs which propagate along the dislocation lines leading to dislocation climb along the surface of the particles [1]. Wherefore, we employed a dislocation density combined with job density based model by [11] to reflect the climb bypass as the controlled shear rate as:

$$\dot{\gamma}_{climb}^{\alpha} = \begin{cases} 0, & |\tau| < \tau_{climb} \\ \rho_m^{\alpha} f_p \frac{\lambda_p}{r_p} c_{jog} D_s * \sinh\left[\frac{(\tau^{\alpha} - {\tau_{climb}}^{\alpha}) b^2 \lambda_p}{k_B T}\right] * sign(\tau^{\alpha}), & |\tau| \geq \tau_{climb} \end{cases} \tag{37}$$

where $f_p$ is the volume fraction of the γ′ phase, $\lambda_p$ is the average inter-particle spacing and $r_p$ is the average time-dependent particle radius. $c_{jog}$ is the dislocation line jog density, $D_s = 7.7 \times 10^{-14} \exp\left(-\frac{Q_v}{k_B T}\right)$ is the bulk diffusivity. The dislocation line jog density is given by [30]:

$$c_{jog} = \frac{1}{a_{jog}} \exp\left(-\frac{Q_{jog}}{k_B T}\right) \tag{38}$$

where $Q_{jog}$ is the formation energy and $a_{jog}$ is the jog segment length which equals $\frac{v_m}{bd}$ with $v_m$ being the atomic volume, and d is the interplanar spacing of slip planes. And the total resistance of climb in slip system α can be given as:

$${\tau_{climb}}^{\alpha} = {\tau_{rc}}^{\alpha} + \mu G b \sqrt{{\rho_{climb}}^{\alpha}} \tag{39}$$

## 2.4. MODEL CALIBRATION

The constitutive formulations are written as a user-defined material (UMAT) subroutine and implemented into Abaqus software. The simulation model is meshed with $10 \times 10 \times 10$ elements and mesh type is C3D8R as shown in Figure 1. Period boundary conditions (PBC) are imposed onto the model. The dislocation density model for both tensile and creep conditions during plastic deformation are calibrated by comparing both the stress-strain curve and creep strain curve with experimental results.

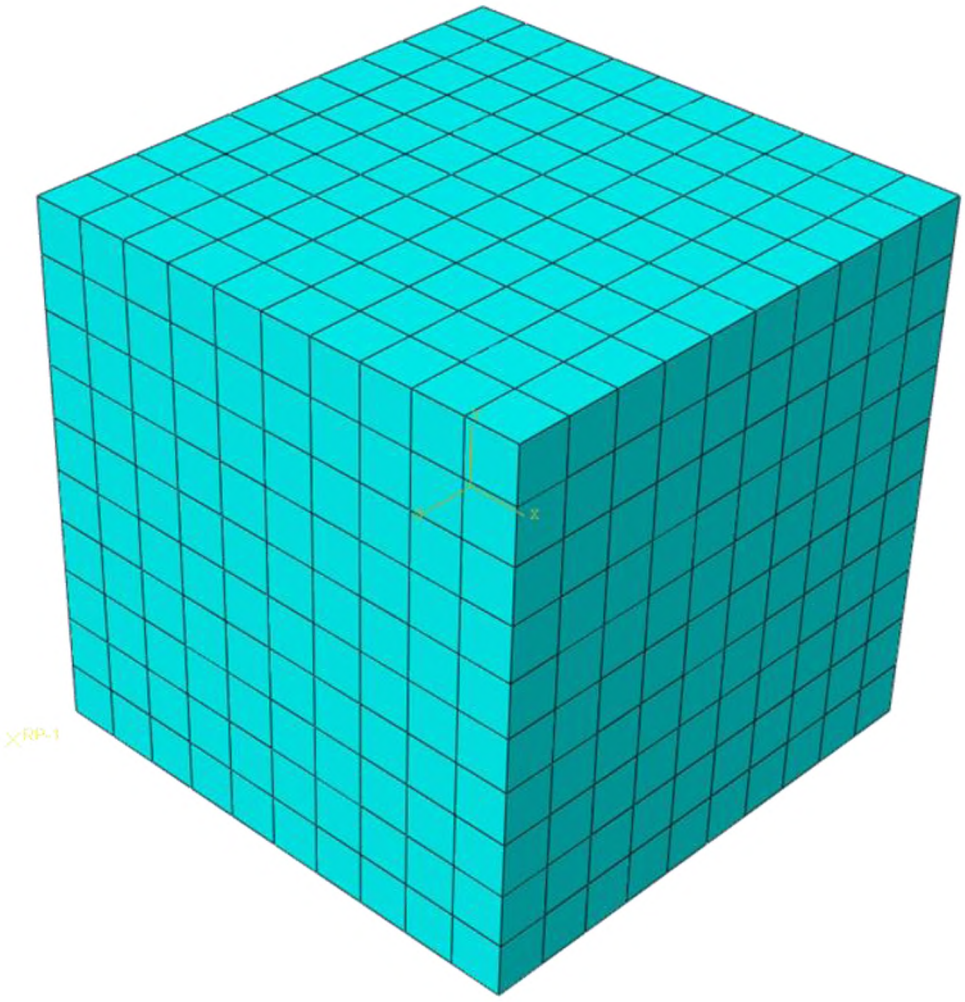

Figure 1. Schematic of the initial finite element mesh.

For tensile condition, the simulated results of Haynes 282 at room temperature (RT), $815^0C$ with applied constant strain rate $\dot{\varepsilon} = 1 \times 10^{-4}s^{-1}$ along X direction, which is the same test condition as the experiment [11]. For the creep condition, the simulated creep tests are conducted under $760^0C$ and $788^0C$ with different loading stress. From Figure 2, we can see that our model are in good agreement with the experiment results, the materials parameters used in our model are listed in Table 2.

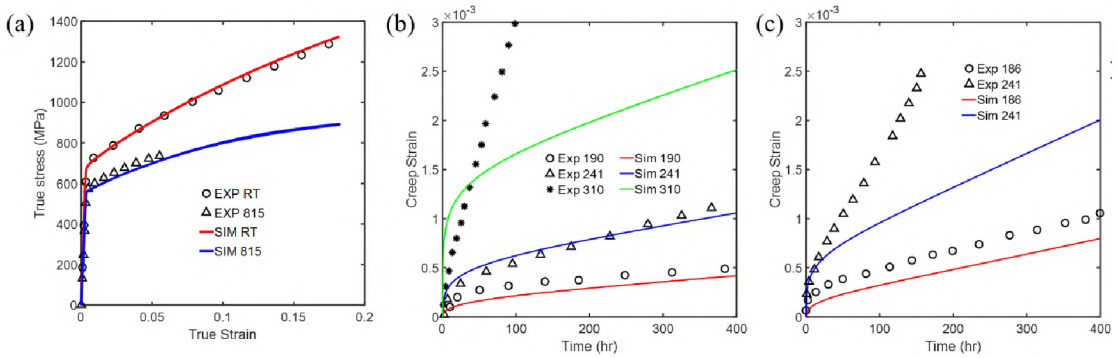


Figure 2. (a) Comparison between simulated and experimental tensile stress-strain curve at RT and 815℃ with an applied shear strain rate of $1\times10^{-4}$ $s^{-1}$(b) Comparison between simulated and experimental creep curves subjected to different tensile stress 190MPa, 241MPa, 310Mpa at 760℃. (c) Comparison between simulated and experimental creep curves subjected to different tensile stress 186MPa, 241MPa at 788℃.

Table 2. Parameters of dislocation-density based CPFE model for tensile and creep behavior of Haynes 282.

| Symbol | Value | Meaning |
|---|---|---|
| $Q_{slip}$ | $3.7\times10^{-19}$ J | Activation energy for slip |
| $Q_{jog}$ | $1.60218\times10^{-19}$ J | Jog formation energy |
| $f_p$ | 0.11 | Volume fraction |
| $v_0$ | $7.8\times10^{11}$ | Attack frequency |
| $Q_v$ | $4.1\times10^{-19}$ J | Bulk diffusion energy |
| $\eta$ | 0.65 | Spatial-distribution parameter |
| $k_1$ | $3.0\times10^{9}$ $m^{-1}$ | Coefficient for statistical trapping of mobile dislocations |
| $\chi$ | 0.15 | Dislocation interaction factor |

Table 2. Parameters of dislocation-density based CPFE model for tensile and creep behavior of Haynes 282. (cont.)

| | | |
|---|---|---|
| μ | 1.0 | Climb dislocation interaction factor |
| b | $2.54 \times 10^{-10}$nm | Magnitude of Burger's vector |
| $g$ | $5.0 \times 10^{-2}$ | Effective activation enthalpy |
| $\tau_D$ | 3300 MPa | Drag stress |
| $\dot{r}$ | $1.0 \times 10^{7}$ $s^{-1}$ | Characteristic rate |
| $\gamma_{APB}$ | 0.18 J | Anti-phase boundary energy |
| $\beta_{for}$ | 0.01 | Constant relate to the spacing of forest dislocation |
| $\beta_{GND}$ | 1.0 | Constant relate to the spacing of GND |
| $\beta_p$ | 0.55 | Constant relate to the spacing of precipitates |

# 3. RESULTS AND DISCUSSION

## 3.1. EFFECT OF TEMPERATURE ON TENSILE PERFORMANCE OF HAYNES 282

From the stress strain curve as shown in Figure 2a, we could observe that the flow stress of Haynes 282 is decreasing with temperature increase, as the flow stress at RT is larger than that of 815 ℃. And also, the strain hardening rate of Haynes 282 at RT is relatively larger compared with that of 815 ℃, illustrating the temperature sensitivity of the strengthening mechanisms like many other Ni-based superalloy. Further, the difference of the flow stress at various temperature levels are increasing with the strain

level. Figure 3 displays the comparison of the flow stress at strain level of 0.05, between the prediction and experiment results. The predicted flow stress is in good agreement with the experiment measurements at different temperature levels. The flow stress at RT is about 905 MPa and greater than that at 815 ℃ with value of 710 MPa. To further investigate the effect of temperature, Figure 4 shows the contribution of each different strengthening terms at different temperatures at the same strain level, we can find that most strengthening terms are decreased as temperature raised from RT to 815 ℃. Especially for the Orowan stress, which is decreasing from about 372.8 MPa to 280.9 MPa. In contrast, the shearing stress and solid solute stress are not displaying tremendous drop as increasing temperature. Due to the short period of the tensile test, the sample will not be expecting any significant change of its composition at various temperature, resulting in the almost the same solid solute stress at both RT and 815 ℃. For shearing stress, at both RT and 815 ℃, it has smaller value compared with Orowan stress, implying shearing stress is performing as the dominant mechanisms during the interaction between dislocation and precipitates. Besides, shearing stress at 815 ℃ is still maintained at a relatively equivalent level as at RT, which is consistent as demonstrated from previous studies saying that shearing stress is acting as the main contributor to the strengthening of Ni-based superalloys during deformation [1]. Strain hardening induced by forest dislocation density is falling from 45.27 MPa to 29.84 MPa as the temperature increase from RT to 815 ℃.

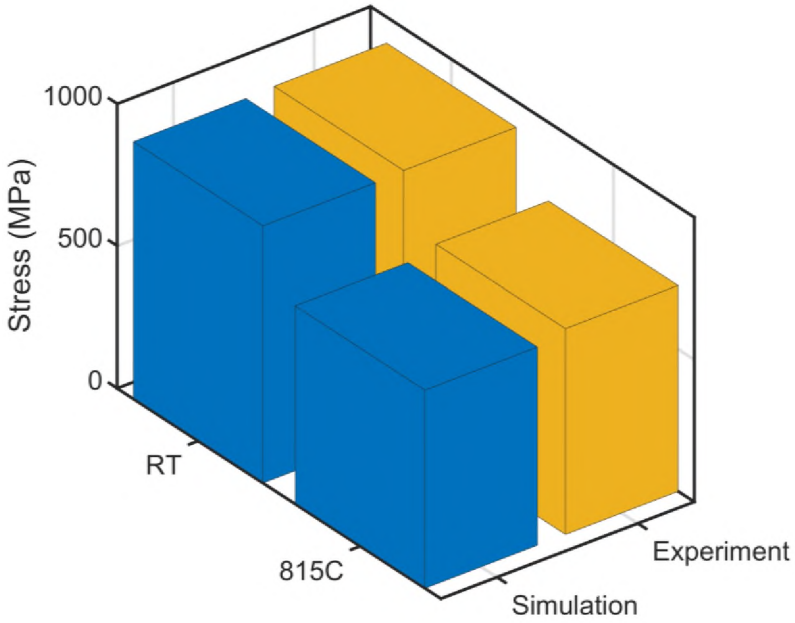


Figure 3. Comparison of the flow stress at strain level of 0.05 between RT and 815℃.

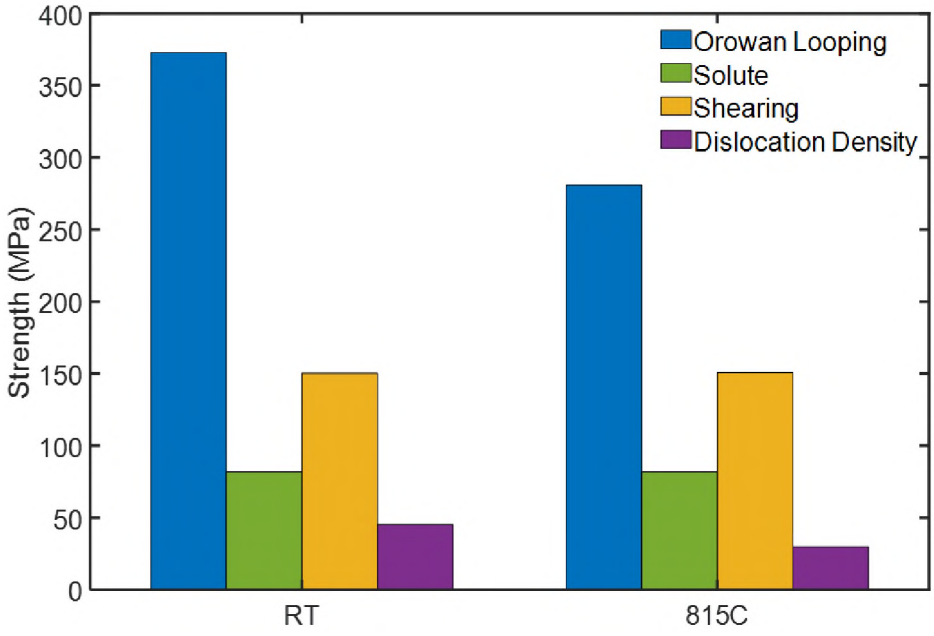


Figure 4. Distribution of the contribution of different strengthening mechanisms at RT and 815℃.

The evolution of the dislocation density with strain is shown in Figure 5, displaying strong temperature. Larger amount of forest dislocation are accumulated in the matrix during deformation at RT than that of 815 ℃ illustrated in Figure 5(a), as thermal energy can help the pinned dislocation segments to overcome their energy barrier allowing rest of dislocations to bow out [18]. Mobile dislocation density, following the principle of maximum plastic dissipation during the plastic deformation, scales with the immobile dislocation density and displayed in Figure 5(b).

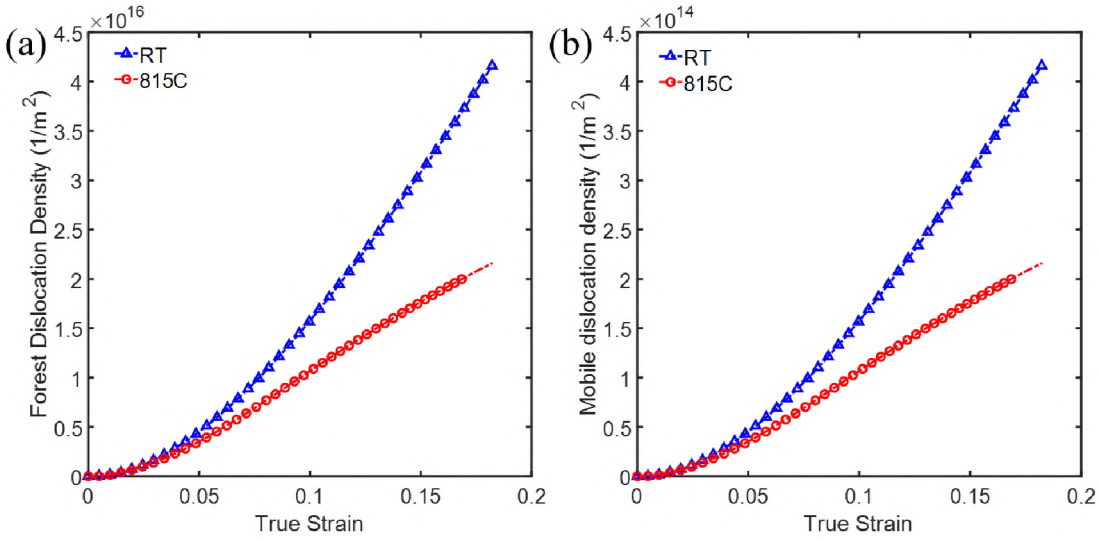


Figure 5. Evolution of the (a) forest dislocation density and (b) mobile dislocation density at RT and 815℃.

### 3.2. DOMINANCE OF EFFECTIVE SPACING

Under such a condition with the development of various dislocation density in the matrix, transition among the interior structure acting as the dominant hindrances can be expected. To record the development of the dominant mechanisms determining the effective spacing of obstacles, the surface plot of the evolution of the effective spacing

are shown in Figure 6. As the deformation process, the increment of GND and forest dislocation density are contributed from the strain incompatible across the grains and the interaction of dislocations, respectively. By scrutinizing the trend of the surface, the surface is declining as the development of forest dislocation density and GND. That said, the effective spacing is decreasing as the process of plastic deformation. And the reduction amount due to the forest dislocation density is larger than that of GND. As the value of forest dislocation density is much larger compared with GND due to the relative tiny strain gradient across grains in Ni-based superalloy compared with other composites like heterogeneous structures, which has large amount of GND as the combination of different grain size level [13, 14]. Therefore, the amount of forest dislocation density is expected to have relatively larger influence in determining the effective spacing of obstacles during the deformation process. Briefly, the spacing of the precipitates particles is acting as the main obstacles to the dislocation motion due to the small amount of dislocation density stored in the matrix at the beginning of the plastic deformation. Later on, large amount of dislocation accumulated in the matrix generated by the interaction of dislocations as the plastic deformation evolves, constructing various substructures and diminishing the spacing of the obstacles for dislocation motion. Temperature level is not showing significant influence on the development of effective spacing as comparing Figure 6(a), (b) and Figure 6(c), (d). Effective spacing at RT is smaller than that of 815 ℃, as the forest dislocation density is larger at low temperature level as shown in Figure 5(a).

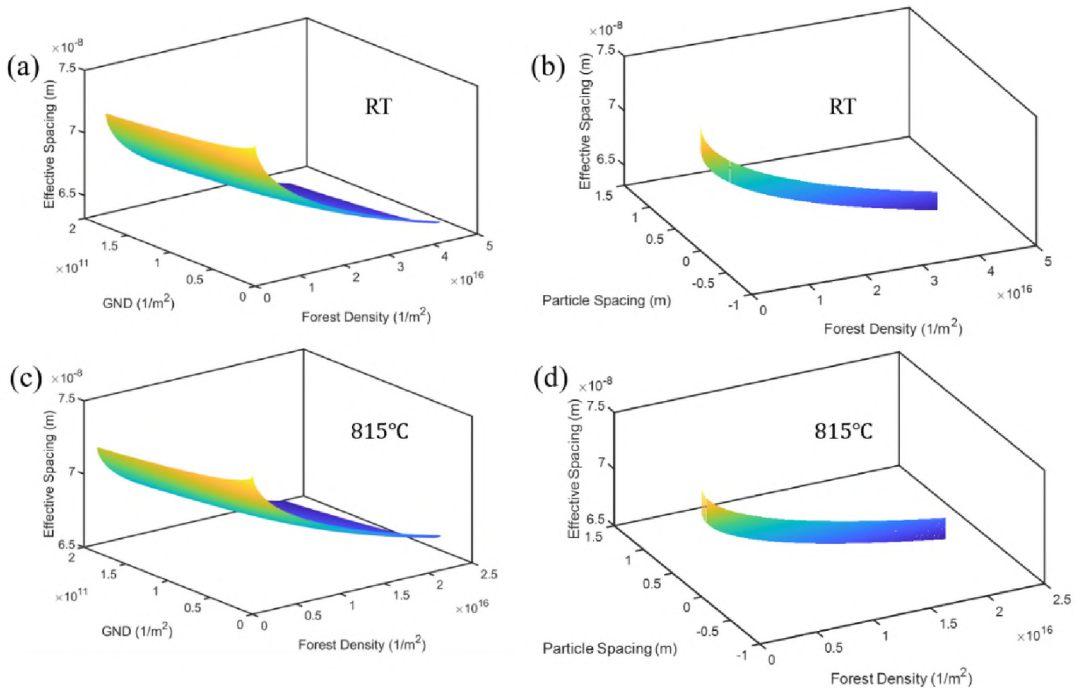


Figure 6. Evolution of the effective spacing with various competing obstacle spacing during the tensile deformation at (a), (b) RT and (c), (d) 815℃.

### 3.3. EFFECT OF $\gamma'$ PRECIPITATES SIZE

Heat treatment from previous studies has been demonstrated that has significant influence on the tensile properties due to the different microstructure. However, little variance of heat treatment will result in a lot of change of microstructural constituents, including the size of particles, precipitates volume fraction, and interconnected carbides. With the advantage of CPFE, which allows our model to quantitatively investigate the effect of different factors. Particle size is one of the most important factors that tremendously influencing the tensile properties of Haynes 282. In our study, we compare the tensile properties of Haynes 282 with two different particle size 15nm and 25nm. Figure 7 (a) shows the stress strain curve at RT and 815 ℃ for both particle size. At 815 ℃, the stress strain curve of 25nm is higher than that of 15nm, illustrating particle with

size of 25nm is taking higher flow stress compared with particle with size of 15nm. To further inspect the change of the flow stress as increasing the particle size, the components of CRSS are compared, including the shearing stress and the stress caused by the development of dislocation density as shown in Table 3.

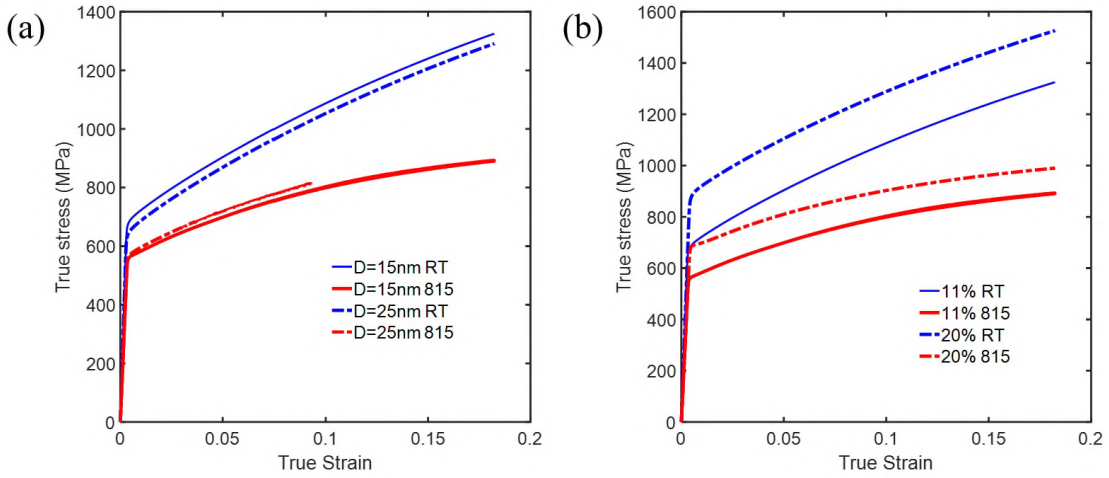


Figure 7. Stress-strain curve of Haynes 282 at RT and 815℃. (a) The effect of precipitates size of 15nm and 25nm, (b) The effect of volume fraction of precipitate phase of 11% and 20%.

Table 3. Values of shearing stress and forest dislocation density induced stress with the effective spacing at different temperature for multiple precipitate size.

| | $\tau_{shear}$ (MPa) | $\tau_{forest}$ (MPa) | $\lambda_{eff}$(nm) |
|---|---|---|---|
| 15nm, RT | 150.30 | 133.95 | 73.03 |
| 15nm, 815 °C | 151.34 | 80.10 | 76.80 |
| 25nm, RT | 157.38 | 126.28 | 124.5 |
| 25nm, 815 °C | 157.36 | 52.28 | 124.9 |

We can find that the increment of shearing stress as the increasing of particle size is the main contributor to the higher strength of particle size of 25nm. In contrast, the stress strain curve is having the conversely trend at RT. The stress with particle size of 15nm is larger than that of 25nm. Similarly, we compare the components stress of CRSS at RT, the shearing stress of larger particle size is larger than that of smaller particles, which is consistent with the observation at 815 ℃. Based on this, we can predict that it must be some other particle size dependent term that has more influence on tensile stress than the component stress of CRSS at RT level. We investigate the effect spacing of obstacles at both particle size and found that the effective spacing with particle size of 25 nm is much larger than that of 15nm. The larger the effective stress, the larger of the equivalent reference shear strain rate will be, which will induce the decrease of the flow stress, and resulting in the lower stress strain curve of 25nm particles.

### 3.4. EFFECT OF $\gamma'$ VOLUME FRACTION

Another important feature that has substantial influence on the tensile property is the volume fraction of the $\gamma'$ phase (add references here). As the $\gamma'$ volume fraction is typically below 20% for Haynes 282. Figure 7(b) shows the stress strain curve taking 11% and 20% volume fraction of $\gamma'$ phase at RT and 815 ℃. As noted in the Figure 7(b), the higher stress is exhibited on the one taking larger amount of $\gamma'$ phase for both RT and 815 ℃ temperature level. High volume fraction of $\gamma'$ will induce larger critical stress for shearing through the precipitates. Furthermore, the extent of the increment of the flow stress is higher for RT than 815 ℃ when increasing the volume fraction.

### 3.5. CREEP BEHAVIOR

The creep tests have been conducted under different loading and temperature conditions as shown in Figure 2(b) and (c). Experimental creep curve shows increasing creep rate, which is likely caused by the microstructure damages such as voids nucleated on the grain boundaries (GB). In present study, we focus on the correlation between the creep strain and the $\gamma/\gamma'$microstructure evolution. The creep strain is increasing with the time at all different stresses and temperature levels. The creeping curves display a fast creep rate at the beginning of the creep time, and then decrease to a certain constant creep rate as demonstrated by a linear increase with time. Two different stages with different creep rate are representing the primary and secondary creep stage, respectively, with the period of the primary creep stage is much shorter than that of secondary creep. Various loading are applied during the creep tests, including 190 MPa, 241 MPa, and 310 MPa at 760 ℃ and 186 MPa and 241 MPa at 788 ℃. At both temperatures, it can be found that higher stress level would cause faster creep rate resulting in larger creep strain during the same period. These phenomenon are consistent with the observation from most of previous studies that the primary creep strain increases with the applied stress and gives way to secondary creep eventually after the knee of the creep curve [1]. Larger stress will trigger the slip systems as the resolves shear stress (RSS) is larger than CRSS, dislocation motion will be stimulated to carry plastic deformation as the form of creep strain. On the other side, at the same stress level, higher temperature will promote the creep strain accumulation due to the promotion of the thermally activated processes.

## 3.6. CLIMB CONTRIBUTION DURING CREEP

In Section 2.3.1, it has been introduced that the climb resistance in our study is consists of the critical stress forming general climb and the stress generated by the deposited climb dislocation density on the coherent particles. To examine the contribution of each process to the climb during the creep process, the evolution of the climb dislocation density gives an outlook to comprehend, which is plotted as revealed in Figure 8. In Figure 8, the climb dislocation density with and without precipitates coarsening are revealed and combined with the evolution of the particle size as the creep time at both 760 ℃ and 788 ℃. At both temperature levels, the climb dislocation density presents a fast growing during the beginning of the creep stage. Since during this short period, the climb dislocation density is low, and the resistance of the climb is mainly contributed via general climb. As the climb dislocation density is increased, the resistance from the deposited climb dislocation density is raising, inducing the slowing down of the growing of the climb dislocation density. At each temperature, stress is showing a strong influence on the accumulation of the climb dislocation density, higher stress will promote larger climb dislocation density deposited on the particles. In other words, higher applied stress will facilitate the dislocation to overcome the precipitates via climb, which proves the well acknowledged fact that the main driving force of the climb is the applied stress from another perspective. Besides, at about equivalent applied stress levels, higher temperature reveals larger amount of climb dislocation density and also exhibits higher increasing rate of the climb dislocation density after the knee of the curve. This phenomenon can be attributed to the fact that thermally activation process would benefit the dislocation climb over the obstacles.

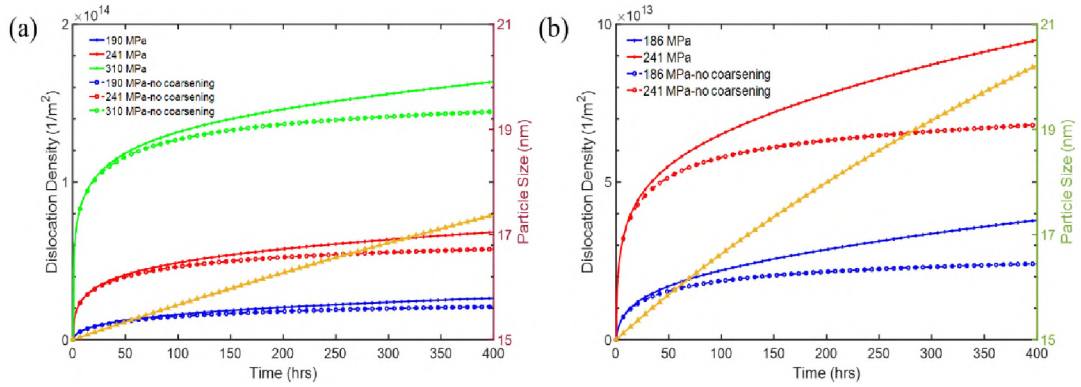


Figure 8. Evolution of deposited climb dislocation density with and without considering particle coarsening at (a) 760 ℃ and (b) 788 ℃.

Figure 9 demonstrations the pie charts of each component of the total resistance of climbing at different applied stress and temperatures levels. Left column are representing the critical stress for each component at 10 hours, which is assumed to be the transition of the primary stage to secondary, and the right column are corresponding the critical stress of each component at 400 hour. By comparing the left column pie charts with those on right column, we can see the slice of deposited dislocation network (yellow color) are having increasing ratio from 10 hour to 400 hour, illustrating the increasing of the climb dislocation density, namely, the increasing of the climb activities. What's more, larger applied stress is found to have higher ratio of the deposited dislocation network at both creep time of 10 hour and 400 hour, demonstrating that larger applies stress will promote the climb activities compared with those at lower stress level. Likewise, at the equivalent stress level, 788 ℃ is unveiling higher ratio of deposited network than 760 ℃, indicating that higher temperature is another important feature that could help to increase the climb happenings.

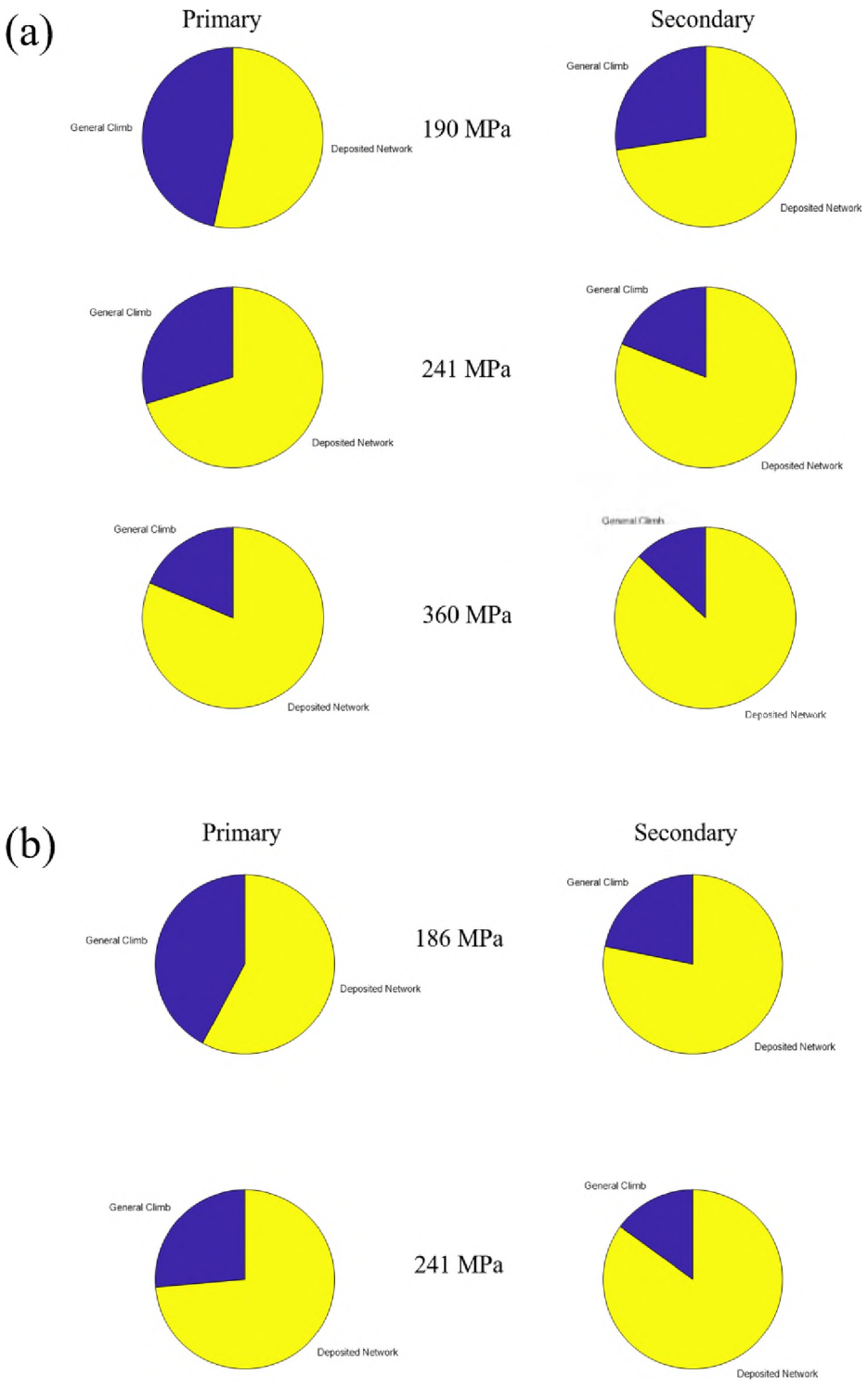


Figure 9. Pie charts displaying each component to the total climb resistance at different stage during creep, with General Climb (blue color) and Deposited Dislocation Network (yellow color) at (a) 760 ℃ and (b) 788 ℃.

### 3.7. EFFECT OF PARTICLES COARSENING

γ′ coarsening has been widely characterized in crept sample of Haynes 282 [10]. Figure 10 compares the creep curves with and without particles coarsening at different temperature and applied stress levels. Samples without coarsening are showing smaller creep strain than those cases with particle coarsening. In other words, particles coarsening can relax the climb resistance during creeping process, as those cases are presenting higher creep strain. And the difference between them are getting larger especially after the knee of the curve. In addition, Figure 8 displays that the climb dislocation density of sample with precipitates coarsening is higher than that of precipitates without coarsening, illustrating that coarsening of precipitates can slow down the climb resistance, and promoting the accumulation of the deposited climb dislocation density.

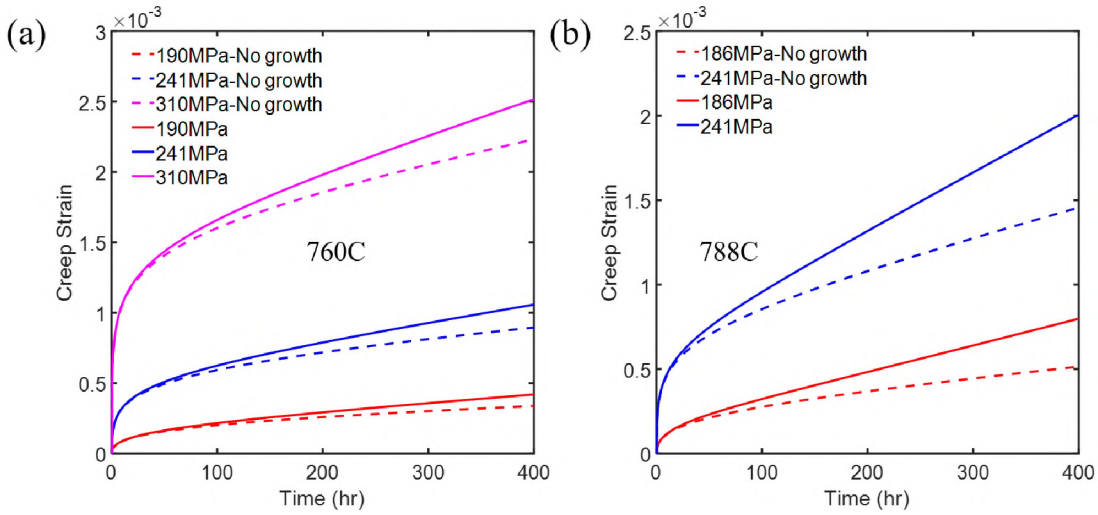


Figure 10. Creep strain curve of Haynes 282 with precipitates coarsening (solid lines) and without precipitates coarsening (dash lines) at 760 °C and (b) 788 °C.

What's more, it is proved that temperature is playing important role in the coarsening of particles, as the particles radius at 788 ℃ is about 20nm, which is larger than the radius at 760 ℃ of 17.3nm. Therefore, at the same applied stress level, dislocation climb is relatively easier at higher temperature, which can be proved that under 241MPa stress loading, the climb dislocation density at 788 ℃ is higher than that at 760℃.

## 4. CONCLUSIONS

In summary, we present a crystal plasticity finite element model for Haynes 282 that account for both the tensile and creeping behavior at different conditions by developing a physical dislocation-density based model. We show that the predicted stress-strain curves at different temperature and creep strain-time curve at various stress and temperature levels agree well with the experimental measurement. In the tensile deformation, most deformation mechanisms are incorporated to embody the real microstructure evolution based on the preset transition of the dominant deformation mechanisms. Moreover, a novel deposited dislocation based model is developed combined with the general climb model for the creeping process. Our results indicate that relatively higher stress and higher temperature will promote the climb process inducing larger climb dislocation density accumulated onto the $\gamma'$ precipitates. This work benefits understanding of the fundamental deformation observed in Hanyes 282 during the tensile and creep tests, and whilst the model can efficiently predict the performance under

various working conditions and assist the optimize process of developing Ni-based superalloys.

## ACKNOWLEDGMENTS

This work was supported by the grants from DOE-NETL Crosscutting Research Program (No. FE0031554).

## REFERENCES

1. Reed, R.C., *The superalloys: fundamentals and applications*. 2008: Cambridge university press.

2. Keshavarz, S. and S. Ghosh, *Multi-scale crystal plasticity finite element model approach to modeling nickel-based superalloys.* Acta Materialia, 2013. **61**(17): p. 6549-6561.

3. Crudden, D., et al., *Modelling of the influence of alloy composition on flow stress in high-strength nickel-based superalloys.* Acta materialia, 2014. **75**: p. 356-370.

4. Haghighat, S.H., G. Eggeler, and D. Raabe, *Effect of climb on dislocation mechanisms and creep rates in $\gamma'$-strengthened Ni base superalloy single crystals: A discrete dislocation dynamics study.* Acta Materialia, 2013. **61**(10): p. 3709-3723.

5. Ali, M.A., J.V. Görler, and I. Steinbach, *Role of coherency loss on rafting behavior of Ni-based superalloys.* Computational Materials Science, 2020. **171**: p. 109279.

6. Cancho, D.B., *Segregation-assisted creep in nickel-based superalloys: experiments, theory and modelling*. 2017, University of Oxford.

7. Zhang, P., et al., *Tensile properties and deformation mechanisms of Haynes 282 at various temperatures.* Metallurgical and Materials Transactions A, 2018. **49**(5): p. 1571-1578.

8. Shin, K.-Y., et al., *Effects of heat treatment on the microstructure evolution and the high-temperature tensile properties of Haynes 282 superalloy.* Materials Science and Engineering: A, 2019. **751**: p. 311-322.

9. Joseph, C., C. Persson, and M.H. Colliander, *Influence of heat treatment on the microstructure and tensile properties of Ni-base superalloy Haynes 282.* Materials Science and Engineering: A, 2017. **679**: p. 520-530.

10. Song, X., et al., *Micro-mechanism during long-term creep of a precipitation-strengthened Ni-based superalloy.* Journal of Materials Science, 2017. **52**(8): p. 4587-4598.

11. Zhao, P., et al., *Heterogeneous $\gamma'$ microstructures in nickel-base superalloys and their influence on tensile and creep performance.* International Journal of Plasticity, 2018. **109**: p. 153-168.

12. Chen, T., et al., *Predicting the size scaling in strength of nanolayered materials by a discrete slip crystal plasticity model.* International Journal of Plasticity, 2020. **124**: p. 247-260.

13. Chen, T. and C. Zhou, *Crystal plasticity modeling the deformation in nanodomained heterogenous structures.* Journal of Materials Research, 2019. **34**(9): p. 1555-1563.

14. Chen, T. and C. Zhou, *Effect of the grain size and distribution of nanograins on the deformation of nanodomained heterogeneous nickel.* Materials Letters, 2019. **236**: p. 661-664.

15. Chen, T., et al., *Crystal Plasticity Modeling of Void Growth on Grain Boundaries in Ni-Based Superalloys.* JOM, 2019. **71**(11): p. 3859-3868.

16. Marin, E. and P. Dawson, *On modelling the elasto-viscoplastic response of metals using polycrystal plasticity.* Computer methods in applied mechanics and engineering, 1998. **165**(1-4): p. 1-21.

17. Mecking, H. and U. Kocks, *Kinetics of flow and strain-hardening.* Acta Metallurgica, 1981. **29**(11): p. 1865-1875.

18. Beyerlein, I. and C. Tomé, *A dislocation-based constitutive law for pure Zr including temperature effects.* International Journal of Plasticity, 2008. **24**(5): p. 867-895.

19. Birosca, S., et al., *The dislocation behaviour and GND development in a nickel based superalloy during creep.* International Journal of Plasticity, 2019. **118**: p. 252-268.

20. Ma, A., F. Roters, and D. Raabe. *A dislocation density based constitutive model for crystal plasticity FEM.* in *Materials Science Forum*. 2005. Trans Tech Publ.

21. Zhu, Z., et al., *A model for the creep deformation behaviour of nickel-based single crystal superalloys.* Acta Materialia, 2012. **60**(12): p. 4888-4900.

22. Goodfellow, A., *Strengthening mechanisms in polycrystalline nickel-based superalloys.* Materials Science and Technology, 2018. **34**(15): p. 1793-1808.

23. Topuz, A.I., *Dimension reduction of defect properties for application in 2D dislocation dynamics.* Computational materials science, 2014. **95**: p. 13-20.

24. Keller, C. and E. Hug, *Kocks-Mecking analysis of the size effects on the mechanical behavior of nickel polycrystals.* International Journal of Plasticity, 2017. **98**: p. 106-122.

25. Roters, F., D. Raabe, and G. Gottstein, *Work hardening in heterogeneous alloys—a microstructural approach based on three internal state variables.* Acta materialia, 2000. **48**(17): p. 4181-4189.

26. Galindo-Nava, E., L. Connor, and C. Rae, *On the prediction of the yield stress of unimodal and multimodal $\gamma'$ Nickel-base superalloys.* Acta Materialia, 2015. **98**: p. 377-390.

27. Feltham, P., *Solid solution hardening of metal crystals.* Journal of Physics D: Applied Physics, 1968. **1**(3): p. 303.

28. Gypen, L. and A. Deruyttere, *Multi-component solid solution hardening.* Journal of Materials Science, 1977. **12**(5): p. 1028-1033.

29. Mishima, Y., et al., *Solid solution hardening of nickel—role of transition metal and B-subgroup solutes—.* Transactions of the Japan institute of metals, 1986. **27**(9): p. 656-664.

30. Hirth, J.P., J. Lothe, and T. Mura, *Theory of dislocations*. 1983, American Society of Mechanical Engineers Digital Collection.

31. Zhao, J., et al., *Dislocation-based modeling of long-term creep behaviors of Grade 91 steels.* Acta Materialia, 2018. **149**: p. 19-28.

32. Quek, S.S., Y. Xiang, and D.J. Srolovitz, *Loss of interface coherency around a misfitting spherical inclusion.* Acta materialia, 2011. **59**(14): p. 5398-5410.

33. Shen, C., *Modeling Creep-Fatigue-Environment Interactions in Steam Turbine Rotor Materials for Advanced Ultra-supercritical Coal Power Plants*. 2014, General Electric Global Research, Niskayuna, NY (United States).

# II. CRYSTAL PLASTICITY MODELING OF VOID GROWTH ON GRAIN BOUNDARIES IN NI-BASED SUPERALLOYS

Tianju Chen[1], Ridwan Sakidja[2], Wai-Yim Ching[3], Caizhi Zhou[1*]

[1] Department of Materials Science and Engineering, Missouri University of Science and Technology, Rolla, MO 65409, USA

[2] Department of Physics, Astronomy and Materials Science, Missouri State University, Springfield, MO 65897, USA

[3] Department of Physics and Astronomy, University of Missouri Kansas City, Kansas City, MO, 64110, USA

## ABSTRACT

In this work, we explore the effect of misorientation angles of crystal orientations between two grains along the grain boundary (GB) on void growth behavior in polycrystalline Ni-based superalloys by using a crystal plasticity finite element method. Quantitative analysis is conducted to study the coupled roles of the crystal orientation and stress triaxiality in void growth in bicrystals. Based on our simulation results, we find that, as the main loading axis perpendicular to the GB, voids grow slower on tilt GBs in bicrystals than those in single crystal and bicrystal samples with twist GBs. While the void growth in single crystal and bicrystal samples with twist GBs exhibited almost the same rate and increased with the stress triaxiality levels. The interaction between two

* Corresponding author.

E-mail address: zhouc@mst.edu

crystals bonded with the GB alert the effective Schmid Factors (SFs) in each crystal that results in asymmetric distribution of the equivalent plastic strain around the void and induces distinct irregular shaped voids during deformation.

**Keywords**: Crystal plasticity; Superalloy; Void growth; Crystallographic orientation

## 1. INTRODUCTION

Polycrystalline Ni-based superalloys are widely used in power generation turbines, due to their good formability, balanced high temperature corrosion and fatigue resistance [1]. In polycrystalline Ni-based superalloys, the small precipitates on grain boundary (GB) can stabilize and strengthen the GB to prevent the GB sliding during the service, and large precipitated phases within the grain can balance the strengths between grain boundaries and grains to improve the durability, ductility, and long-term high temperature stability [2, 3]. However, precipitations on the GB may act as the hotspots for void nucleation in polycrystalline Ni-based superalloy under external loading due to the high stress concentration at the interface between the hard precipitates and the matrix [4]. Generally, the damage and failure of polycrystalline Ni-based superalloys typically exhibit well-defined three-stage behaviors [5]: the nucleation of voids around the inclusions or the second phase particles, void growth and coalescence under external loading, which leads to the initiation of macroscopic cracks and fracture in the material. Thus, understanding the void behavior, especially on GBs, is critical for processing those alloys with desired mechanical properties for multiple applications.

Numerous efforts have been put in place to develop predictive model for the void growth and coalescence in ductile materials. The pioneering work by Rice and Tracey [6] revealed the important role of stress triaxiality in the void growth and they also developed the R-T model for spherical void embedded in an infinite solid. In order to consider the interaction between adjacent voids, Gurson proposed the plastic potential of the rigid-perfectly plastic material with voids based on a cell model, and developed a more sophisticated constitutive relationship between the macroscopic flow behavior and remote stress fields [7]. To better understand the stress and strain distributions around voids during the growth and coalescence, Tvergaard and Needleman carried out finite element analysis (FEA) employing the modified Gurson's constitutive relationship and reproduced the cup-cone fracture in a round tensile specimen [8]. Following the original 2-D FEA works by Tvergaard and Needleman, an axisymmetric cylindrical model was developed to explore the real 3-D void growth under various combinations of triaxial loadings [8]. After that, more accurate body centered cubic model and cubic primitive model were used on analyzing the damage by void growth in ductile materials [9]. In general, the axisymmetric cylindrical model predicts a larger deformation in the solid with voids that a lower value of the material failure stress than cubic cell models. Although various modifications have been made to the foregoing models, there are still considerable mismatches between predicted and experimental results [10, 11].

To accurately predict the damage process of ductile materials under complex loading history, the characteristics of microstructural changes and the anisotropic properties of materials need to be considered. Crystal plasticity finite element model (CPFEM) has been used in recent studies to explore the mechanisms of void growth and

coalescence in ductile metals, as it is a full-field model that considers the anisotropy of materials and various microstructure features relevant to the plastic deformation in crystalline materials. With this advantage, CPFEM has been employed since long time ago based on its exceptional capacities dealing with the void growth behavior in single crystals [12, 13]. Shu et al. [14] studied the void growth in a single crystal under uniaxial and biaxial strain fields by using an elasto-viscoplastic strain gradient crystal plasticity formulation. They found that small voids are less susceptible to growth than large voids, which is consistent with the results from the study by Tvergaard and Niordson [15]. Wen et al. [16] explored the void size effects on the yield surfaces in metallic materials based on the extended the Gurson's model with the Taylor dislocation theory. Their modeling results revealed that the influence of the void on the stress-strain curves gradually becomes significant as the initial void volume fraction increase. Orsini and Zikry [17] analyzed the void growth in FCC copper single crystals by using a rate-dependent crystal plasticity model and claimed that the lattice rotation and slip mainly concentrated in the regions between the voids for only one crystal orientation. Portirniche et al. [18] probed the effects of crystal orientation on the void growth and coalescence in FCC single crystals under uniaxial and biaxial loading by using 2D CPFE analysis. They demonstrated that in the case of uniaxial tension, the void growth strongly depends on the angle between the crystal orientation and the direction of the stretching axis, while the influence from crystal orientations is negligible for the void coalescence. Under the biaxial tension, the void growth and coalescence did not depend on the crystal orientation but the stress triaxiality in FCC single crystals. Yu et al. [19] explored the void growth in Ni-based single crystal superalloys under monotonically increasing loading. Their results

illustrated that low stress triaxiality promotes the change of the void shape, while high stress triaxiality mainly induces the void expansion. Although, numerous studies have shown that the crystal orientation and stress triaxiality may affect the void growth in single crystalline materials, there is little information available in the literature regarding the void growth on GBs and it is still unclear how the GB affect the void growth on GBs and whether the existing micro-mechanical model derived from the single crystalline materials can rationally predict the void growth on GBs.

In this study, we perform CPFE calculations to explore the effect of GB types (both tilt and twist) and GB misorientation angles (low to high) on the void growth on the GBs in polycrystalline Ni-based superalloys and also quantify the relationships between the stress triaxiality and void growth in polycrystalline Ni-based superalloys.

## 2. METHODOLOGY

A crystal elasto-viscoplastic model and the corresponding integration scheme is used in this study [20]. In this model, the kinematics of crystal deformation is based on the multiplicative decomposition of the deformation gradient $\boldsymbol{F}$:

$$\boldsymbol{F} = \boldsymbol{F_e F_P} \tag{1}$$

where $\boldsymbol{F_e}$ and $\boldsymbol{F_p}$ are the elastic and plastic gradients, respectively. The plastic component evolves as:

$$\dot{\boldsymbol{F}}_{\boldsymbol{P}} = \boldsymbol{L_P F_P} \tag{2}$$

$\boldsymbol{L_P}$ is the velocity gradient, which accounts for the plastic deformation generated by the plastic shear strain rate on different slip systems:

$$\boldsymbol{L_P} = \sum_{\alpha=1}^{N} \dot{\gamma}_\alpha \, \boldsymbol{b}^\alpha \boldsymbol{n}^\alpha \tag{3}$$

where $\boldsymbol{b}^\alpha$ and $\boldsymbol{n}^\alpha$ are the slip direction and slip plane normal on slip system $\alpha$, $\dot{\gamma}_\alpha$ is the shear strain rate on slip system $\alpha$, and $N$ is the total number of slip systems in the crystalline material. The corresponding shear strain rate in slip system $\alpha$ is calculated with the power-law equation:

$$\dot{\gamma}^\alpha = \dot{\gamma}_0 \left(\frac{|\tau^\alpha|}{\tau_c^\alpha}\right)^{\frac{1}{m}} sgn(\tau^\alpha) \tag{4}$$

where $\dot{\gamma}_0$ is a reference shear strain rate, $\tau^\alpha$ and $\tau_c^\alpha$ are resolved shear stress (RSS) and shear resistance for the plastic flow in the slip system $\alpha$, respectively, and $m$ is the strain rate sensitivity exponent.

In our model, we employ the Voce-hardening law to calculate the evolution of the shear resistance for each slip system [21],

$$\dot{\tau}_c^\alpha = \sum_\beta h_{\alpha\beta} \, |\dot{\gamma}^{(\beta)}| \tag{5}$$

where $h_{\alpha\beta}$ is the strain hardening modulus, and can be expressed as:

$$h_{\alpha\beta} = q_{\alpha\beta} h \tag{6}$$

$q_{\alpha\beta}$ are the interaction coefficients that represent the effect of the hardening between different slip systems, and $h$ is the self-hardening modulus. The evolution of the self-hardening modulus is formulated as [22]:

$$h(\gamma_\alpha) = h_s + \left[h_0 - h_s + \frac{h_0 h_s \gamma_\alpha}{\tau_s - \tau_0}\right] exp^{-\frac{h_0 \gamma_\alpha}{\tau_s - \tau_0}} \tag{7}$$

$h_0$ is the initial hardening modulus, $\tau_0$ is the initial yield shear stress, $\tau_s$ is the saturation yields shear stress, $h_s$ is the saturation hardening modulus at large strains, and $\gamma_\alpha$ is the acculated shear strain in all slip systems, given by:

$$\gamma_\alpha = \int_0^t \sum_\alpha |\dot{\gamma}^{(\alpha)}| \, dt \tag{8}$$

The crystal plasticity constitutive equations are written as a user-defined material (UMAT) and implemented into Abaqus CAE. As Inconel 718 with an FCC structure is one of the most common polycrystalline Ni-based superalloys with high operating temperature and low cost, we adopt the modeling parameters for Inconel 718 which were calibrated and validated by Cruzado et al. [21] in our calculations and listed in Table. 1.

Table 1. Parameters used in CPFE model for IN718.

| $C_{11}$ (GPa) | $C_{12}$ (GPa) | $C_{44}$ (GPa) | $\tau_0$ (MPa) | $\tau_s$ (MPa) | $h_0$ (GPa) | $h_s$ (GPa) | $q_{\alpha\beta}$ |
|---|---|---|---|---|---|---|---|
| 259.6 | 179 | 109.6 | 465.5 | 598.5 | 6.0 | 0.3 | 1 |

In this study, we use a cube model to represent the unit cell and the void is set at the center of the unit cell as shown in Figure 1. The total number of elements in the model is 6128 elements and an eight-node brick finite element with reduced integration (C3D8R) is used. Similar model and mesh have also been used to study the void growth in single crystal samples in recent CPFE work [23]. The length of each side is set equal to 1 and the initial void radius is 0.13365 that makes the initial void volume fraction, $f_0$, equal to 0.01. Under the external loading, the central point on each surface can only move in the normal direction. Meanwhile, all six surfaces are constrained to remain flat using MPC (multi-point constraints), i.e. the displacement of a surface is coupled with a master

node which controls the slave nodes on the surface. Therefore, there is no shear on each surface, and the displacement on along each axis can be represented as:

$$L_1 = L_{10} + U_1, L_2 = L_{20} + U_2, L_3 = L_{30} + U_3 \tag{9}$$

The macro-strain of the cell model along each axis is

$$E_1 = \ln\left(\frac{L_1}{L_{10}}\right), E_2 = \ln\left(\frac{L_2}{L_{20}}\right), E_1 = \ln\left(\frac{L_3}{L_{30}}\right) \tag{10}$$

And the macro-equivalent strain is calculated by

$$E_e = \frac{\sqrt{2}}{3}\sqrt{(E_1 - E_2)^2 + (E_2 - E_3)^2 + (E_3 - E_1)^2} \tag{11}$$

The overall stresses are imposed onto each surface, and in order to maintain a constant stress triaxilaity in each calculation, the ratio of axial normal stress imposed on each surface is set to be a constant during the deformation,

$$\sum 2 = \rho_2 \sum 1, \qquad \sum 3 = \rho_3 \sum 1 \tag{12}$$

where $\rho_2$ and $\rho_3$ are both constants. The macroscopic effect stress$\sum e$, and the macroscopic hydrostatic stress, $\sum h$ are given by

$$\sum e = \frac{1}{\sqrt{2}}\sqrt{(\sum 1 - \sum 2)^2 + (\sum 2 - \sum 3)^2 + (\sum 3 - \sum 1)^2} \tag{13}$$

$$\sum h = \frac{1}{3}(\sum 1 + \sum 2 + \sum 3) \tag{14}$$

The stress triaxiality, $T$, is then calculated as following

$$T = \frac{\sum \mathrm{h}}{\sum \mathrm{e}} = \frac{\frac{\sqrt{2}}{3}(1+\rho_2+\rho_3)}{\sqrt{(1-\rho_2)^2+(\rho_2-\rho_3)^2+(\rho_3-1)^2}} \tag{15}$$

In order to systematically analyze how the stress triaxilaity affect the void growth on GBs, four different stress triaxilaity are used in our calculations: 0.33, 0.5, 1.0 and 2.0.

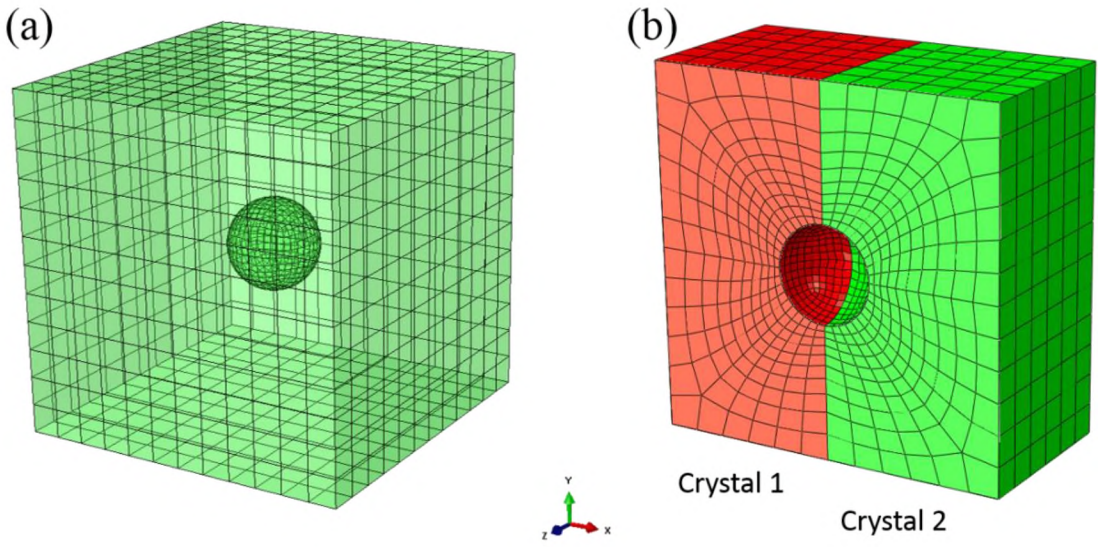


Figure 1. The initial finite element mesh for void growth calculations (a) the whole model, (b) cross-section of the meshed sample with the void at the center of the simulation box (Two different colors represent two different crystallographic orientations.).

To create twist and tilt GBs in our calculations, we assign Crystal 1 (the original crystal) in the bicrystal sample with the [001] orientation, and then create Crystal 2 by rotating Crystal 1 along the X-axis and Z-axis for the twist and tilt GBs, respectively. Two different rotation angles, 15° and 45°, are used to create low angle and high angle GBs, which normally possess low and high GB energies and affect the material properties of metals significantly [24]. The main loading direction is along x-axis, which is perpendicular to the GB.

# 3. RESULTS AND DISCUSSION

## 3.1. VOID GROWTH IN SINGLE CRYSTALS

Figure 2 (a) shows the growth of the void volume fraction in single crystal samples versus macroscopic equivalent strain at different stress triaxiality levels. The growth of the void volume fraction is defined as $f/f_0$ [25], where $f$ is the porosity which is taken as the difference between the instantaneous cell volume and the total elemental volume in its instantaneous configuration. As a result, stress triaxiality prompts to an amplification of void growth rate with increasing strain level, which is consistent with the theory proposed by Rice and Tracey [6]. Figure 2 (b)-(e) exhibit the deformed void shapes in single crystal samples at $E_e = 0.2$. It can be noticed that the shape of deformed voids strongly depends on the magnitude of the stress triaxiality. At lower stress triaxiality level, the void is mainly elongated along the main loading axis with much larger deformation than other lateral directions, inducing the elongated olive shaped voids as depicted in Figure 2 (b) and (c). Despite the void is driven to stretch along the main loading axis at intermediate and high stress triaxiality levels, the ratio of the long to short axes of the void is reduced compared with those for lower stress triaxiality level at the same macro-equivalent strain, as shown in Figure 2 (d) and (e). Our simulation results for single crystal samples are consistent with the results from previous studies [19, 26-28] that larger stress triaxiality levels will promote the void growth along all the tree loading axis that induces the deformed voids almost stay spherical (see Figure 2 (e)).

## 3.2. VOID GRIWTH ON GBS IN BICRYSTALS

To study the effect of GBs on the void growth, we compare the void growth, $f/f_0$, in bicrystal and single crystal samples as shown in Figure 3. For all cases, the void volume fraction increase with the macro-equivalent strain ( $E_e$). In addition, higher stress triaxialities induced larger void growth at the same macro-equivalent strain for cases with the same GB type. The void growth curves for voids in bicrystal samples with twist GBs almost overlap with the curves for pure single crystals, although the void grew slightly faster in samples with twist 45° GBs than those with twist 15°. Compared with twist GBs, the voids on tilt GBs exhibit relative slow growth rate. Among the five different cases, the void on the tilt 45° GBs grew the smallest amount at the macro-equivalent strain $E_e = 0.2$.

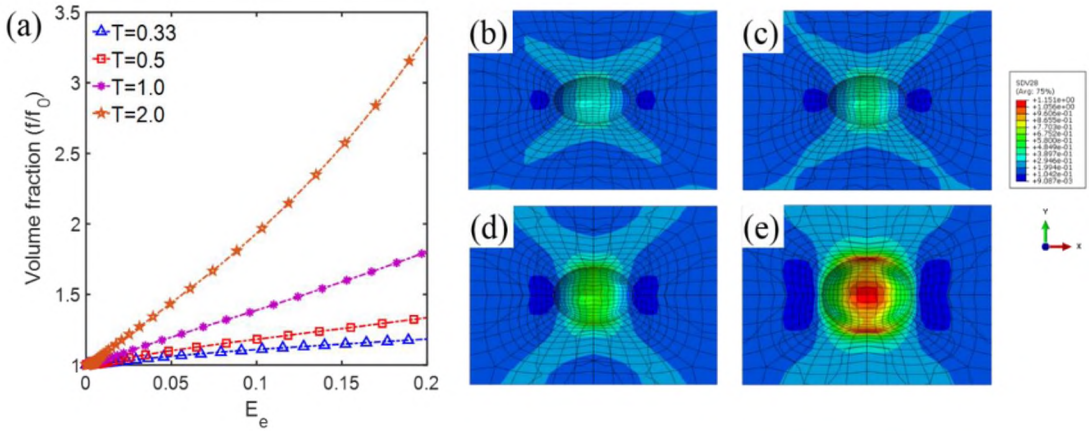


Figure 2. (a) Evolution of the void volume fraction $f/f_0$ versus macro-equivalent strain for void in single crystal under different stress triaxiality levels, T. Distribution of equivalent plastic strain around the void in single crystal samples at $E_e = 0.2$ under (b) $T = 0.33$, (c) $T = 0.5$, (d) $T = 1.0$ and (b) $T = 2.0$.

To make quantitative comparison of the void growth in single crystal and bicrystal samples, we plot the ratio of the difference between the void volume fractions of

bicrystal and single crystal to the void volume fraction of single crystal at $E_e = 0.2$ as shown in Figure 4. It is clear that twist and tilt GBs exhibit opposite effects on the void growth, i.e. the twist GBs promote the void growth, while the tilt GBs inhibit the void growth, as the ratios are all positive and negative for bicrystals with twist and tilt GBs, respectively. Furthermore, the increment of the stress triaxiality amplified those effects, as the ratios possess the largest values at T = 2.0 for all four different bicrystals.

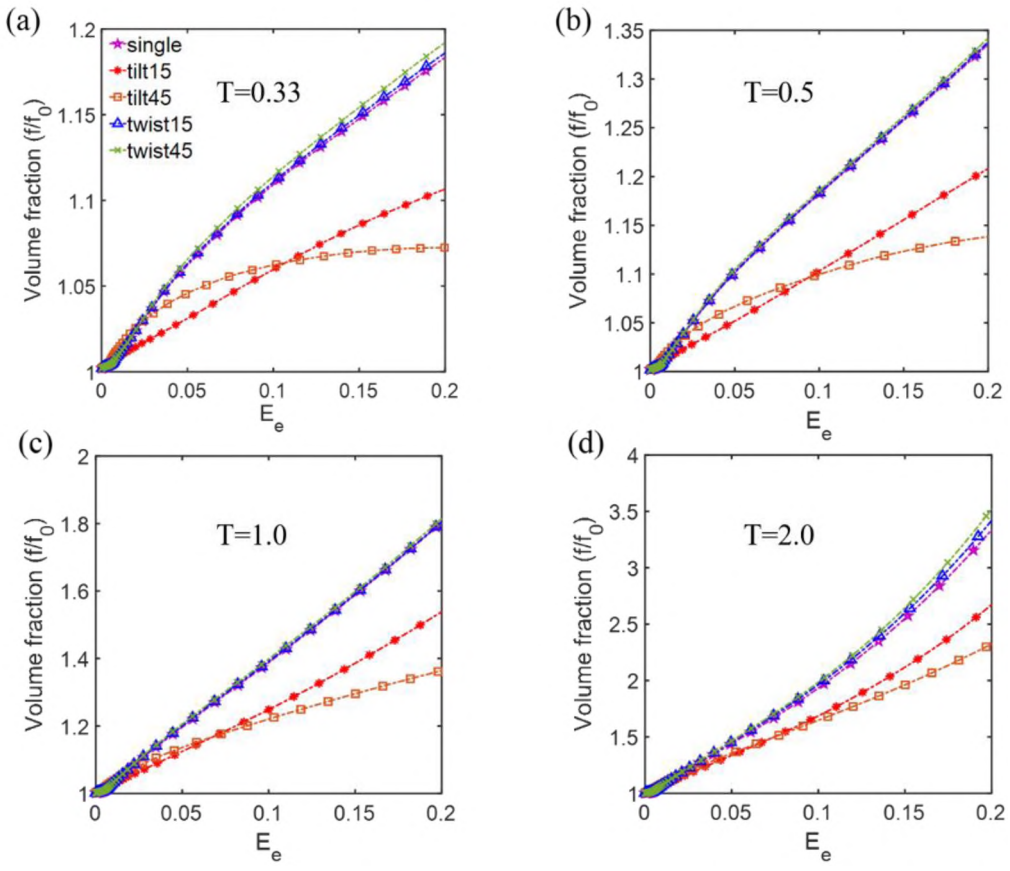


Figure 3. Evolution of the void volume fraction $f/f_0$ versus macro-equivalent strain for void in single crystal and in bicrystal at different stress triaxiality level: (a) T = 0.33, (c) T = 0.5, (d) T = 1.0 and (b) T = 2.0.

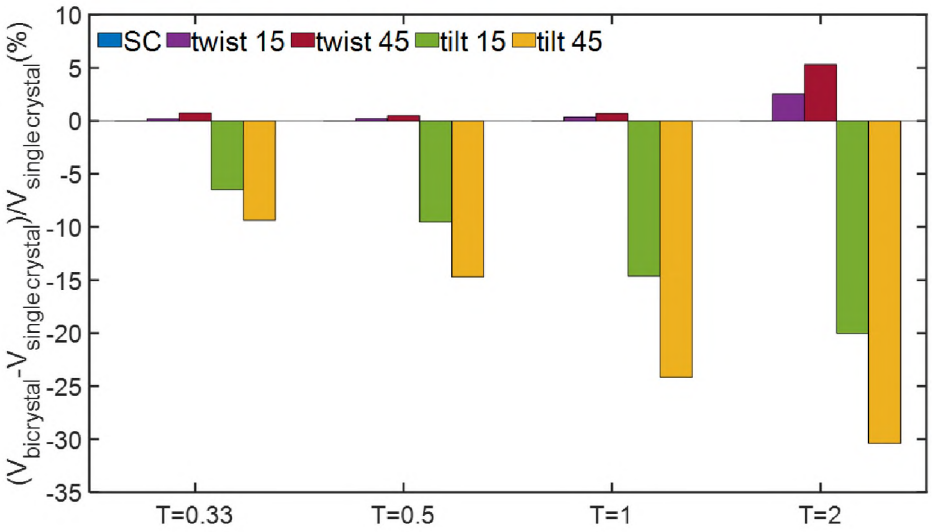


Figure 4. The ratio of the difference between the void volume fractions in bicrystal, $V_{\text{bicrystal}}$, and single crystal, $V_{\text{single crystal}}$, to the void volume fraction of single crystal at $E_e = 0.2$.

## 3.3. PLASTIC DEFORMATION OF BICRYSTALS WITH VOIDS

**3.3.1. Accumulated Shear Strain on Slip Systems.** In order to explore the void expansion behavior on GB in bicrystals, further analysis is provided here by scrutinizing the accumulated shear strain of each slip system in both single crystal and bicrystals. Figure 5 presents the accumulated shear strain on each slip system in Crystal 1 versus the nominal Schmid Factor (SF) for each slip system at $\boldsymbol{E_e = 0.2}$ with various stress triaxiality levels. The nominal SF on each slip system in Crystal 1 is evaluated by using the macro-stress field and initial orientation of each element. Figure 5 illustrates that, the accumulated shear strains are generally large on those slip systems with higher Schmid Factors (SFs). Specifically, at T=0.33, there are eight slip systems among the twelve slip systems generating accumulated shear strain under external applied loading whose nominal SFs are all equal to 0.408, and the accumulate shear strain amount on those eight

slip systems are almost the same equal to 0.125, while there were no plastic shear strain on the other four slip systems with SFs equal to 0. At higher stress triaxiality level T=2.0, larger amount of accumulated shear strain are still accumulated at the slip systems with higher nominal SFs. However, the difference on the accumulated shear strain on the slip systems with low and high SFs has been diminished.

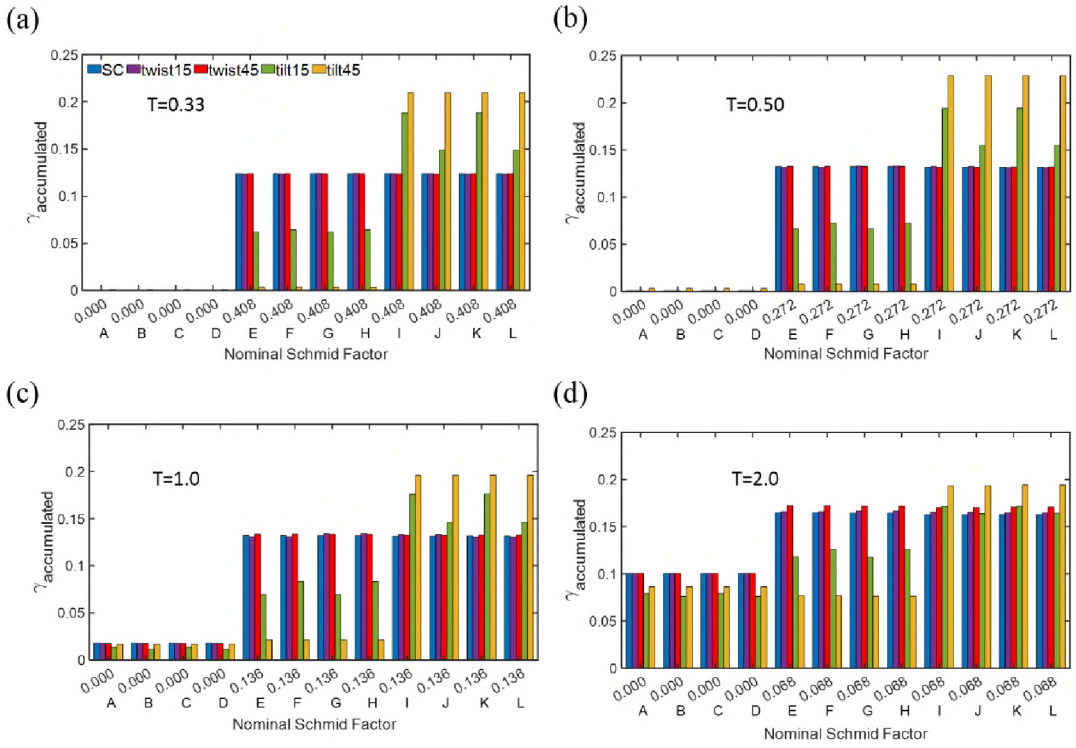


Figure 5. Accumulated shear strain of each slip system versus normal Schmid Factor at $E_e = 0.2$ for different stress triaxiality level: (a) T = 0.33, (c) T = 0.5, (d) T = 1.0 and (b) T = 2.0.

Moreover, in Figure 5, it can also be noticed that the amount of accumulated shear strain on each slip system in Crystal 1 bonded with twist GBs is almost the same as that on the corresponding slip system in single crystal samples. Consequently, the void

growth in bicrystal with twist GBs is almost identical to that in the single crystal sample as shown in Figure 3. In contrast, the accumulated shear strain of Crystal 1 in bicrystal with tilt GBs displays a totally different trend. For instance, at T=0.33, only four out of the eight slip systems with the highest nominal SFs (0.408) provide a certain amount of accumulated shear strain in Crystal 1 bonded with tilt 45° GBs, while there was almost no shear strain accumulating on the other eight slip systems including those four with the highest nominal SFs (0.408). Since only four slip systems are clearly active during the deformation in Crystal 1 bonded with tilt 45° GBs, the magnitude of the accumulated shear strain on those four slip systems are about 65% higher than those on eight active slips in the single crystal sample. Although the eight slip systems with the highest nominal SFs (0.408) were all activated during the deformation in Crystal 1 bonded with tilt 15° GBs, the amount of the plastic strain on those slip systems is different between each other. The magnitude of the accumulated shear strain on four of them is higher than that in the single crystal sample, while the other four slip systems experienced much less shear strain than those in the single crystal sample. Similar phenomena also occurred for other stress triaxiality levels, as significant difference of the shear strain were built up on slip systems with the same nominal SFs. Furthermore, with the stress triaxiality levels increases, the magnitude of accumulated shear strain on the four slip systems (A-D) with initial zero SFs raises in all five cases, and even higher than the accumulated shear strain on some of the slip systems (E-H) with highest nominal SFs at T = 2.0 as shown in Figure 5 (d).

**3.3.2. Lattice Rotation During Void Growth.** As stress triaxiality levels increasing, the loading mode changes from uniaxial tension for T = 0.33 to multiaxial

tension for T > 0.33. Multiaxial tension may generate highly unsymmetrical slip events in twelve slip systems and cause the lattice rotation during the deformation [29]. Figure 6 presents the distributions of the misorientation angle of each element in the single crystal sample along the main loading axis at $E_e = 0.2$. We can see that the misorientation distribution is getting broader as the stress triaxiality level rises from 0.33 to 2.0. It indicates higher stress triaxiality levels can induce larger lattice rotations. As a consequence of the lattice rotation, the effective SF on each slip system may change. Slip directions with lower SFs may rotate to a direction with higher SFs that promotes plastic strain of the whole sample to satisfy the external applied load. Therefore, slip systems with lower nominal SFs may still provide shear strain during the deformation at high stress triaxiality levels as shown in Figure 5 for single crystal samples.

To exam whether this scenario can be applied to bicrystals, we compare the distributions of misorientation angles of Crystal 1 along the main loading axis at $E_e = 0.2$ in bicrystal samples with T = 0.33 and 1.0 in Figure 6 (b) and (c). We can see that high stress triaxiality levels promote the lattice rotation, as the distribution for each case at T = 1.0 is much wider than that at T = 0.33 and the maximum rotation angle for each case increases by 3 – 5 times from T = 0.33 to 1.0 as shown in Figure 6 (b) and (c). However, it is demonstrated that most elements in Crystal 1 only were rotated by a very small angle, as the peaks of the distributions in Figure 6 (b) and (c) locating between 0° and 5°, even for T = 1.0. Such small rotations cannot significantly change the values of SFs and affect the plastic deformation and accumulate shear strain on each slip system in the crystalline materials. Thus, based on the values of nominal SFs, it is hard to explain the huge difference on the accumulated shear strain between the slip systems E-H and I-L shown in

Figure 5, all of which hold the highest nominal SFs among the twelve slip systems for different stress triaxiality levels.

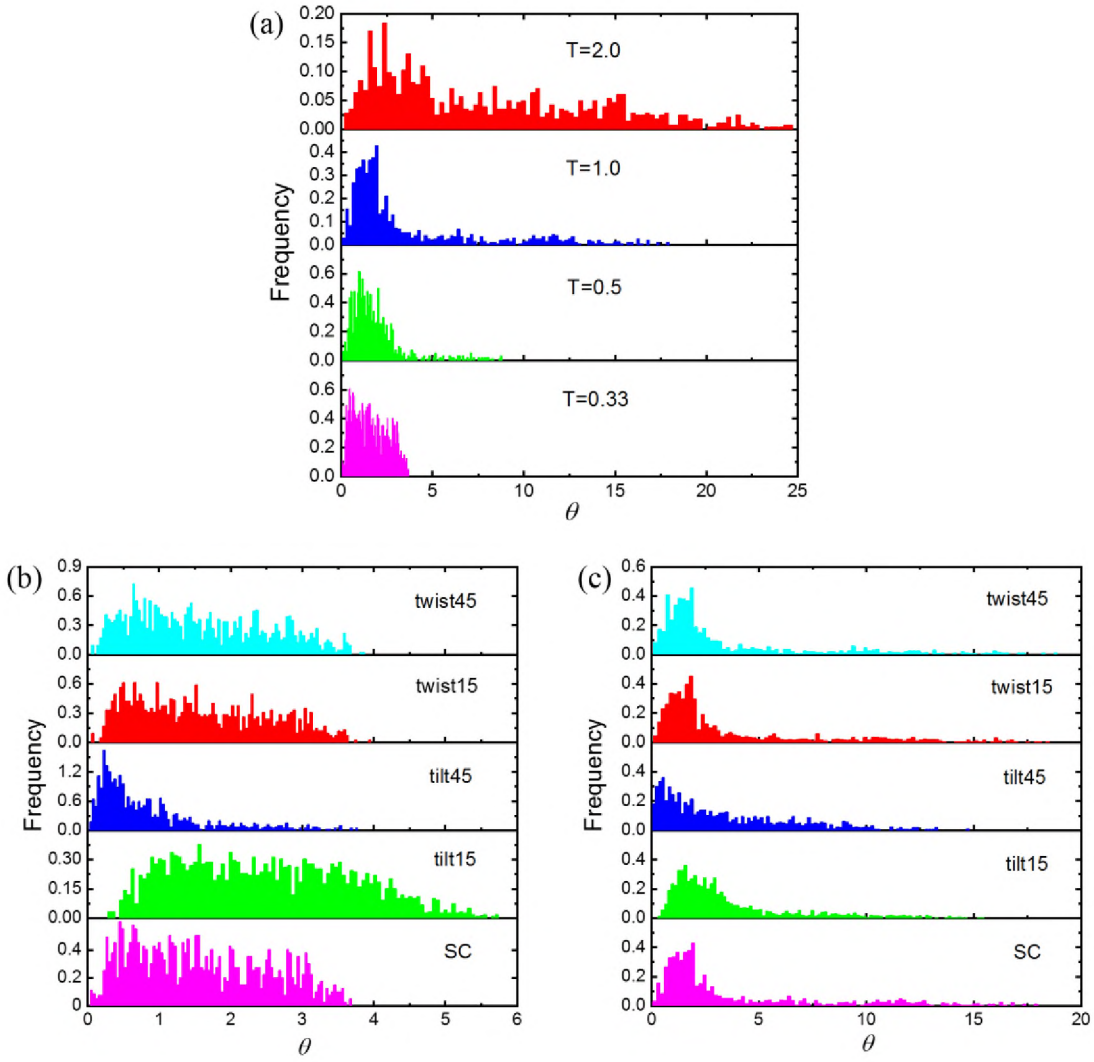


Figure 6. Distribution of misorientation angles of elements at $E_e = 0.2$ in (a) single crystal samples, (b) bicrystal samples for T = 0.33 and (c) T = 1.0.

**3.3.3. Effective Schmid Factors.** As the crystallographic orientations of the Crystal 1 and Crystal 2 in bicrystals are different, their mechanical responses to external loading will be dissimilar to each other [30]. With this, we can anticipate that the interaction between Crystal 1 and Crystal 2 will alter the local stress field within both of them and drive them away from the applied macro-stress status. As a result, the effective SFs on each slip system during the deformation in Crystal 1 may deviate from the nominal SFs and facilitate the plastic shear strain accumulating on slip systems with low SFs. With the advantage of the CPFE model, we obtained the effective SF on each slip system in Crystal 1 at $E_e = 0.2$ and plot them versus the nominal SF in Figure 7.

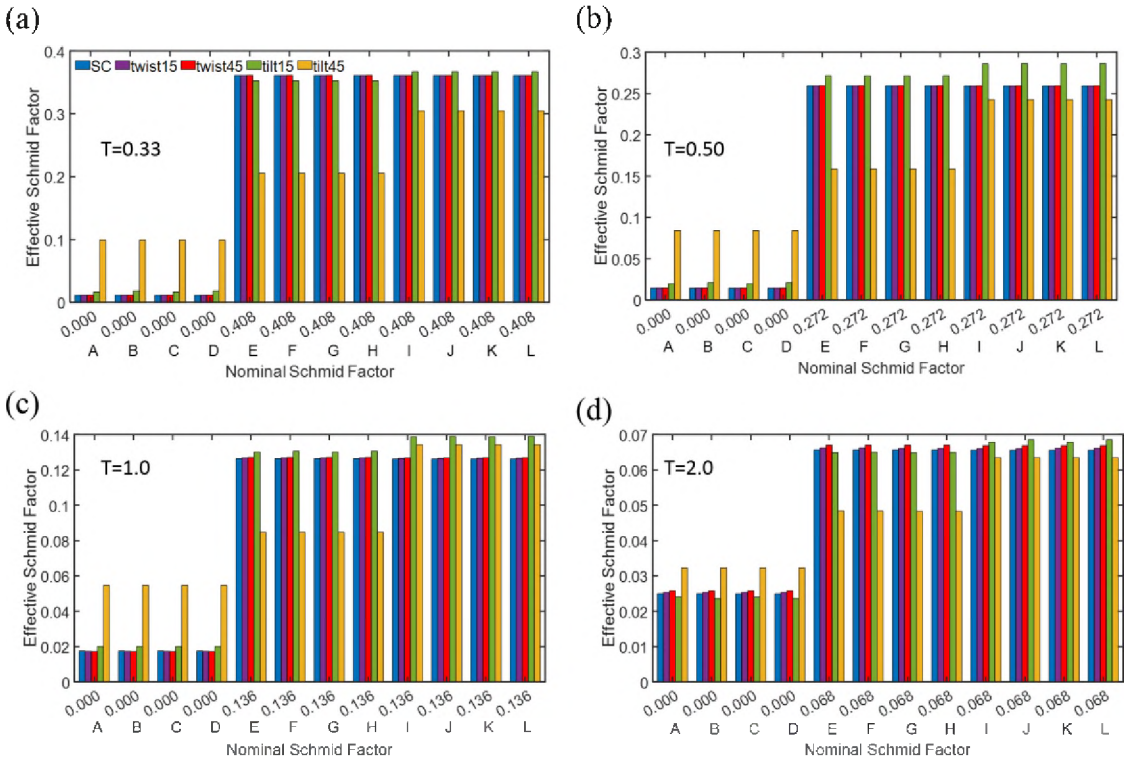


Figure 7. Effective Schmid Factors for each slip system versus normal Schmid Factors at $E_e = 0.2$ for (a) T = 0.33, (c) T = 0.5, (d) T = 1.0 and (b) T = 2.0.

For all four different T values, the slip systems A-D with nominal SFs equal to 0 possess effect SFs larger than 0, the values of which increased with stress triaxiality levels. In addition, the differences on nominal SFs between the slip systems with the lowest SFs and the highest SFs are about 0.408 and 0.068 for T = 0.33 and 2.0, respectively. These differences are much smaller in effective SFs with the values equal to about 0.35 to 0.03 for T = 0.33 and 2.0. For the slip systems E-H with the highest nominal SFs, their effective SFs are obviously decreased due to the interaction between the Crystal 1 and Crystal 2. This significant difference between nominal and effective SFs shown in Figure 7 explains the trend of the accumulated shear strain observed in Figure 5.

### 3.4. VOID SHAPE AND EQUIVALENT PLASTIC STRAIN DISTRIBUTION.

To probe the effect of GBs on the deformation of materials around the void, we compare the distribution of equivalent plastic strain at E_e=0.2 for T=0.33 and T=1 in Figure 8. We can notice that the spherical voids have been stretched along axis parallel to the main loading direction for all single crystal and bicrystal samples, as the voids grow faster along the main loading direction. The largest equivalent plastic strain always occurs near the mid-section along the main loading direction in each case, due to the high stress concentration around the void near the GB. However, in the bicrytals with tilt GBs, the largest equivalent plastic strains are less than those in bicrystals with twist GBs. Moreover, obvious uneven distribution of the equivalent plastic strain are displayed for bicrystal with tilt GBs, especially for the bicrystal with tilt 45° GB, resulting in the asymmetric deformed void shape on both side of GB. Additionally, the deformed void in

Crystal 1 has more expansion extent than that in Crystal 2, and larger stress triaxiality induced larger difference between Crystal 1 and Crystal 2, leading to an irregular shaped void. It is worth to mention that Crystal 1 with [001] orientation was selected as the target crystal for our analysis, as its crystallographic orientation is relative stable without significant lattice rotation during the plastic deformation [31], especially under multiaxial loading.

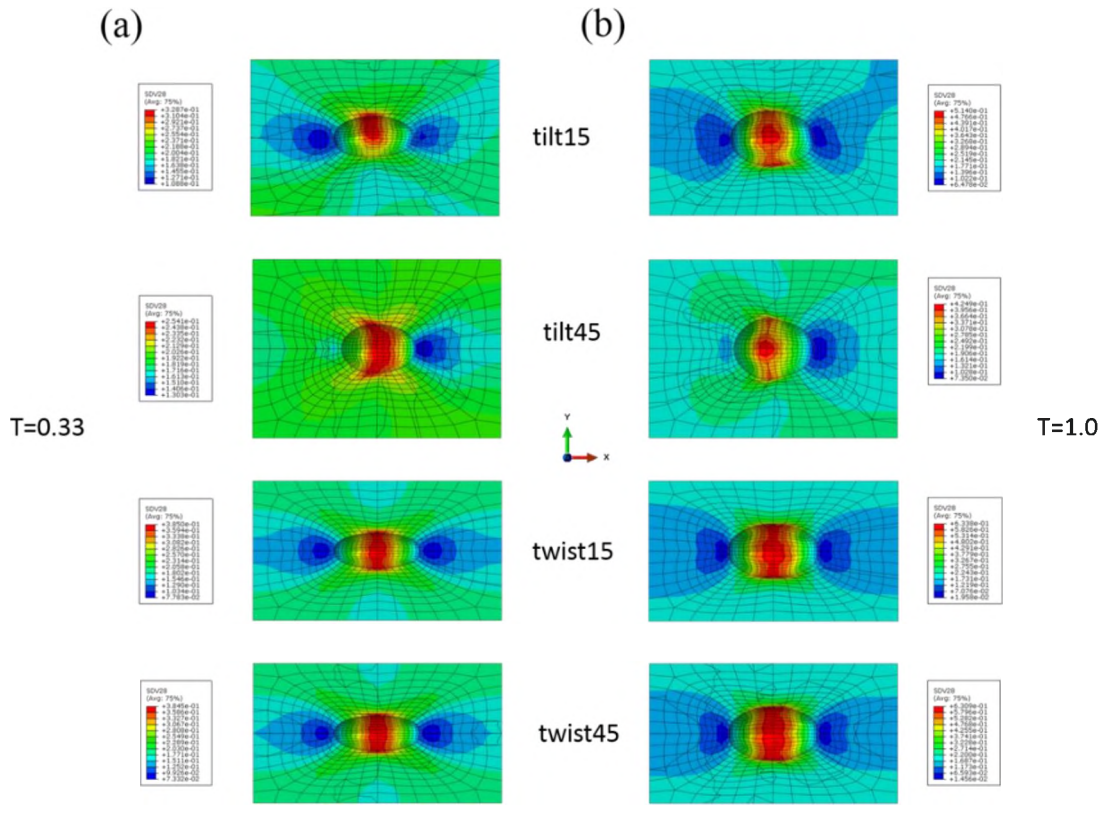


Figure 8. Distribution of equivalent plastic strain around deformed voids at $E_e = 0.2$ for (a) T = 0.33 and (b) T = 1.0.

With this useful feather, it is relative easy to make quantitative comparisons of the lattice rotation and accumulated shear strain on Crystal 1 in single crystal and bicrystal

samples during the void growth. In addition, we assume the GBs in our model is highly intact without deboning and there is no crack or void nucleation on the GBs during the deformation. Under the influence of stress triaxiality, additional nucleation of nanovoids may occur on the interfaces, as observed by recent integrated computational and experimental study [32]. Thus, further works are needed to identify the critical condition for the void nucleation on the GBs, which is another important issue relevant to the deformation and damage of polycrystalline Ni-based superalloy [5]. Despite this shortage of our model, we nevertheless succeeded in identifying the role of GBs and grain-grain interaction on the void growth on different type of GBs with various misorientations.

## 4. CONCLUSIONS

In this study, we explored the effect of GBs on void growth behavior in polycrystalline Ni-based superalloys, and also identified the relationship between the stress triaxiality and void growth in both single crystal and bicrystals by using a crystal plasticity finite element method. Our CPFEM calculation results demonstrated that, voids grow slower on tilt GBs in bicrystals than those in single crystal and bicrystal samples with twist GBs, while the void growth in single crystal and bicrystal samples with twist GBs exhibited almost the same rate and increased with the stress triaxiality levels. In addition, void growth is accompanied with the lattice rotation, and higher stress triaxiality leads to larger lattice rotation. Based on our analysis, the interaction between two crystals bonded with the tilt GB alerted the effective SFs in each crystal that results in asymmetric distribution of the equivalent plastic strain around the void and induced distinct irregular

shaped voids during deformation. This work benefits our understanding of the anisotropic void growth on GBs in polycrystalline Ni-based superalloys and can shed light on the role of crystal orientation mismatch in the damage of ductile polycrystalline materials.

## ACKNOWLEDGMENTS

This work was supported by the grants from DOE-NETL Crosscutting Research Program (No. FE0031554).

## REFERENCES

[1] R.C. Reed, *The Superalloys: Fundamentals and Applications*, (Cambridge, UK:Cambridge university press, 2008), pp. 217-271.

[2] F. Theska, A. Stanojevic, B. Oberwinkler, S.P. Ringer, and S. Primig, *Acta Mater.*, 156, 116 (2018).

[3] Z. Tarzimoghadam, D. Ponge, J. Klöwer, and D. Raabe, *Acta Mater.*, 128, 365 (2017).

[4] T. Gibbons and B. Hopkins, *Met. Sci.*, 18, 273 (1984).

[5] G. Zhu, F. Liu, X. Li, J. Pang, Z. Zhang, P. Li, Y. Zhou, and Z. Zhang, *Adv. Eng. Mater.*, 21, 1800856 (2019).

[6] J.R. Rice, and D.M. Tracey, *J. Mech. Phys. Solid*, 17, 201 (1969).

[7] A.L. Gurson, *J. Eng. Mater. Technol*, 99, 2 (1977).

[8] V. Tvergaard and A. Needleman, *Acta Metall.*, 32, 157 (1984).

[9] M. Kuna and D. Sun, *Int. J. Fatigue*, 81, 235 (1996).

[10] T. Pardoen, I. Doghri, and F. Delannay, *Acta Mater.*, 46, 541 (1998).

[11] Y. Shi, *Eng Fract Mech*, 34, 901 (1989).

[12] T. O'regan, D. Quinn, M. Howe, and P. McHugh, *Comput Mech,* 20, 115 (1997).

[13] D. Quinn, P. Connolly, M. Howe, and P. McHugh, *Int. J. Mech. Sci.*, 39, 173 (1997).

[14] J.Y. Shu, *Int. J. Plast.*, 14, 1085 (1998).

[15] V. Tvergaard and C. Niordson, *Int. J. Plast.*, 20, 107 (2004).

[16] J. Wen, Y. Huang, K. Hwang, C. Liu, and M. Li, *Int. J. Plast.*, 21, 381 (2005).

[17] V. Orsini and M. Zikry, *Int. J. Plast.*, 17, 1393 (2001).

[18] G. Potirniche, J. Hearndon, M. Horstemeyer, and X. Ling, *Int. J. Plast.*, 22, 921 (2006).

[19] Q. Yu, N. Hou, and Z. Yue, *Comput. Mater. Sci.*, 48, 597 (2010).

[20] E.B. Marin, Report No. SAND2006-4170, Sandia National Laboratories, 2006.

[21] A. Cruzado, B. Gan, M. Jiménez, D. Barba, K. Ostolaza, A. Linaza, J. Molina-Aldareguia, J. Llorca, and J. Segurado, *Acta Mater.*, 98, 242 (2015).

[22] C. Tome, G. Canova, U. Kocks, N. Christodoulou, and J. Jonas, *Acta Metall.*, 32, 1637 (1984).

[23] A. Srivastava and A. Needleman, *Mech. Mater.*, 90, 10 (2015).

[24] V.V. Bulatov, B.W. Reed, and M. Kumar, *Acta Mater.*, 65, 161 (2014).

[25] A. Srivastava and A. Needleman, *Modell. Simul. Mater. Sci. Eng.*, 20, 035010 (2012).

[26] S.K. Yerra, C. Tekog˘lu, F. Scheyvaerts, L. Delannay, P. Van Houtte, and T. Pardoen, *Int. J. Solids Struct.*, 47, 1016 (2010).

[27] C. Ling, S. Forest, J. Besson, B. Tanguy, and F. Latourte, *Int. J. Solids Struct.*, 134, 43 (2018).

[28] K.S. Zhang, J.B. Bai, and D. François, *Int. J. Solids Struct.*, 38, 5847 (2001).

[29] M.A. Meyers and K.K. Chawla, *Mechanical Behavior of Materials*, (Cambridge, UK:Cambridge university press, 2008), pp. 381-392.

[30] R.J. Asaro, *Adv. Appl. Mech.*, 23, 1 (1983).

[31] I.J. Beyerlein and L.S. Tóth, *Prog. Mater Sci.*, 54, 427 (2009).

[32] X. Zhang, Y. Mu, M. Dodaran, S. Shao, D. Moldovan, and W.J. Meng, *Acta Mater.*, 160, 1 (2018).

# SECTION

# 3. CONCLUSIONS AND RECOMMENDATIONS

## 3.1. CONCLUSIONS

In this study, the mechanical behavior of Ni-based superalloy is investigated with using Crystal Plasticity Finite Element Method (CPFEM) by evaluating the underlying deformation and damage process. With the advantage of CPFEM, the relationship between the microstructure state and the macroscopic mechanical performance can be associated, by investigating varies quantities based on the developed physical based models and comparing with the experiment measurements. As a consequence of this study, numerous significant conclusions are reportable.

In paper one, a dislocation-density based constitutive model is developed to investigate the deformation mechanisms during the tensile and creep test of Haynes 282. For tensile condition, most of the deformation mechanisms that have been demonstrated to have influence during the deformation are incorporated. The results of tensile test reveals that the strength of the Haynes 282 is heavily dependent on the temperature. Below a certain level of temperature, dislocation shearing through the precipitates is acting as the main contributor to the strength of Haynes 282. Increasing the temperature will alter the critical stress for the activation of dislocation shearing and also produce different dislocation density stored in the matrix inducing different strength at various temperatures. Benefit from CPFEM, the effect of precipitates size and volume fraction can be inspected. Analysis of the results at different precipitate size discloses that larger

precipitate size will increase the resistance of dislocation shearing through the precipitates and decrease the critical stress for dislocation looping around the precipitates. Larger volume fraction of $\gamma'$ will also increase the strength of Haynes 282 at both room temperature (RT) and 815 ℃, as the critical stress are increased required by various strengthen mechanisms. During the creeping process, a dislocation climb controlled shear rate model is established to study the creeping behavior at relatively small stress and high temperature levels. The creep results display that creep strain is increasing much faster at the beginning during the primary stage and slow down to a constant rate through the secondary stage. A novel climb model accounting for the accumulated dislocation density in the vicinity of the particles is developed in this study. It has been found that relatively higher stress and higher temperature will promote the dislocation climb over the $\gamma'$ particles, generating larger climb dislocation density. The dominant climb mechanisms transits from the dislocation general climb to the resistance of deposited dislocation network as the creep process.

In paper two, CPFEM is applied to study the effect of grain boundary (GB) on void growth behavior. Different types of GB are considered, including the twist GB and the tilt GB. The growth behavior of void on different type GBs in bicrystals are compared with the void in single crystal. Results show that larger stress triaxiality will induce larger growth of the voids, and the deformed void shape is strongly dependent on the stress triaxiality levels. In addition, voids on twist GB are almost showing the same growth performance as the voids in the single crystal. However, voids on tilt GBs will suppress the void growth due to much smaller volume fraction than those on twist GBs and single crystal. Shear strain accumulation of voids on tilt GBs are not following the traditional

Schmid law which are calculated by the macroscopic stress state. Further investigation found that the effective Schmid factor has changed from its initial values as a result of the interaction between the two crystals. As a consequence, the void on tilt GBs will be deformed into an irregular unsymmetrical shape.

## 3.2. FUTURE WORKS

Developing newly advanced Ni-based superalloys is critical as the demanding of the superior requirement of the materials to satisfy more extreme conditions. CPFEM as a powerful computational technique is able to predict a variety of character of materials in a significantly efficient manner compared with experimental approach. In the future, CPFEM combined with Machine Learning (ML) can be a reliable method to optimize the materials in order to have superior properties. CPFEM can be used to predict the mechanical performance with different chemical composition, texture and precipitate size and volume fraction, and inhomogeneous distribution of the precipitates. A lot of data generated by CPFEM based on different initial conditions of Ni-based superalloy can then be trained and categorized with using ML. As a result, optimized data can be extracted and forecasted for processing Ni-based superalloys with expected properties.

In addition, in the present study of the void growth behavior on GBs, we assume that the void is nucleated on the GBs with a sphere shape to simplify the model and only focus on the effect of different type of GB on the void growth behavior. In fact, void shape nucleated on the GBs is strongly dependent on the surface energy and strain energy around the void. Also, there is always a second phase precipitate around the nucleated void. Reducing the local energy drives the evolution of the void and determine the void

shape. Multiscale computational approach is a influential method, to determine some fundamental parameters that experiments could not reach. Like DFT, which is able to help to find the strain energy and surface energy near the carbide phase on GB. By setting up the criterion based on the calculation of DFT, CPFEM is able to predict the crack nucleation during the deformation.

# BIBLIOGRAPHY


1. Furrer, D. and H. Fecht, *Ni-based superalloys for turbine discs.* Jom, 1999. **51**(1): p. 14-17.

2. Reed, R.C., *The superalloys: fundamentals and applications*. 2008: Cambridge university press.

3. Cancho, D.B., *Segregation-assisted creep in nickel-based superalloys: experiments, theory and modelling*. 2017, University of Oxford.

4. Vorster, W. and F. Dunne, *Crystal plasticity and multiscale modelling of superalloy creep.* Philosophical Magazine, 2012. **92**(7): p. 830-848.

5. Rae, C. and L. Zhang, *Primary creep in single crystal superalloys: some comments on effects of composition and microstructure.* Materials Science and Technology, 2009. **25**(2): p. 228-235.

6. Goodfellow, A., *Strengthening mechanisms in polycrystalline nickel-based superalloys.* Materials Science and Technology, 2018. **34**(15): p. 1793-1808.

7. Estrada Rodas, E.A., *Microstructure-sensitive creep-fatigue interaction crystal-viscoplasticity model for single-crystal nickel-base superalloys*. 2017, Georgia Institute of Technology.

8. Ma, A., D. Dye, and R. Reed, *A model for the creep deformation behaviour of single-crystal superalloy CMSX-4.* Acta Materialia, 2008. **56**(8): p. 1657-1670.

9. Reppich, B. and G. Schumann, *Electron microscopy of γ' particles in nickel-based superalloys.* Materials Science and Engineering: A, 1988. **101**: p. 171-182.

10. Joseph, C., C. Persson, and M.H. Colliander, *Influence of heat treatment on the microstructure and tensile properties of Ni-base superalloy Haynes 282.* Materials Science and Engineering: A, 2017. **679**: p. 520-530.

11. Jaladurgam, N.R., et al., *Microstructure-dependent deformation behaviour of a low γ' volume fraction Ni-base superalloy studied by in-situ neutron diffraction.* Acta Materialia, 2020. **183**: p. 182-195.

12. Ahmadi, M.R., et al., *Modeling of precipitation strengthening in Inconel 718 including non-spherical γ "precipitates.* Modelling and simulation in materials science and engineering, 2017. **25**(5): p. 055005.

13. Matysiak, H., et al., *Microstructure of Haynes® 282® superalloy after vacuum induction melting and investment casting of thin-walled components.* Materials, 2013. **6**(11): p. 5016-5037.

14. Theska, F., et al., *On conventional versus direct ageing of Alloy 718.* Acta Materialia, 2018. **156**: p. 116-124.

15. Tarzimoghadam, Z., et al., *Hydrogen-assisted failure in Ni-based superalloy 718 studied under in situ hydrogen charging: the role of localized deformation in crack propagation.* Acta Materialia, 2017. **128**: p. 365-374.

16. Shin, K.-Y., et al., *Effects of heat treatment on the microstructure evolution and the high-temperature tensile properties of Haynes 282 superalloy.* Materials Science and Engineering: A, 2019. **751**: p. 311-322.

17. Galindo-Nava, E., L. Connor, and C. Rae, *On the prediction of the yield stress of unimodal and multimodal γ' Nickel-base superalloys.* Acta Materialia, 2015. **98**: p. 377-390.

18. Reppich, B., *Some new aspects concerning particle hardening mechanisms in γ'precipitating Ni-base alloys—I. Theoretical concept.* Acta Metallurgica, 1982. **30**(1): p. 87-94.

19. Reppich, B., P. Schepp, and G. Wehner, *Some new aspects concerning particle hardening mechanisms in γ'precipitating nickel-base alloys—II. Experiments.* Acta Metallurgica, 1982. **30**(1): p. 95-104.

20. Courtney, T.H., *Mechanical behavior of materials*. 2005: Waveland Press.

21. Van Sluytman, J.S., *Microstructure and High Temperature Creep of Platinum Group Metal Modified Nickel Base Superalloys*. 2010.

22. Chen, T., et al., *Crystal Plasticity Modeling of Void Growth on Grain Boundaries in Ni-Based Superalloys.* JOM, 2019. **71**(11): p. 3859-3868.

23. Zhu, G., et al., *Tensile Deformation Behaviors and Damage Mechanisms of SRR99 Superalloy Bicrystals with Different Grain Boundary Misorientations.* Advanced Engineering Materials, 2019. **21**(2): p. 1800856.

24. Chen, T., et al., *Predicting the size scaling in strength of nanolayered materials by a discrete slip crystal plasticity model.* International Journal of Plasticity, 2020. **124**: p. 247-260.

25. Chen, T. and C. Zhou, *Effect of the grain size and distribution of nanograins on the deformation of nanodomained heterogeneous nickel.* Materials Letters, 2019. **236**: p. 661-664.

26. Chen, T. and C. Zhou, *Crystal plasticity modeling the deformation in nanodomained heterogenous structures.* Journal of Materials Research, 2019. **34**(9): p. 1555-1563.

27. Roters, F., et al., *Crystal plasticity finite element methods: in materials science and engineering*. 2011: John Wiley & Sons.

28. Marin, E.B., *On the formulation of a crystal plasticity model*. 2006, Sandia National Laboratories.

29. Yuan, R., *Understanding the deformation mechanisms in nanostructured metals by a novel discrete crystal plasticity finite element model.* 2017.

# VITA

Tianju Chen was born in Luoyang City, Henan Province, China in 1990. He received his bachelor's degree in Mechanical design and Manufacturing and Their Automation in 2013 from Henan University of Science and Technology, Luoyang, Henan, China. During his senior, Tianju was selected as an exchange student studying at Pittsburg State University, Pittsburg, KS, USA, with major in Mechanical Engineering. After that, he chose to stay there and continued his study as a graduate student with major in Mechanical Engineering Technology and obtained his master's degree in 2015. In the fall of 2015, he started his Ph.D. study at University of Missouri in Columbia, MO, USA with major in Mechanical and Aerospace engineering. Driven by the great interest in the area of studying mechanical behavior of materials, Tianju transferred from Mizzou to Missouri University of Science and Technology and continued his PhD program in the spring of 2016. He commenced his work on his doctoral research project on developing Crystal Plasticity Model to study the deformation mechanisms of Ni-based superalloys. He received his Ph.D. in Materials Science and Engineering in August 2020, from Missouri University of Science and Technology.